Numerical investigation of the unsteady distortion for an Sduct intake with mechanical vortex generators

Geoffrey Tanguy, David G Macmanus, Eric Garnier

Numerical investigation of the unsteady distortion for an S-duct intake with mechanical vortex generators

Geoffrey Tanguy[1], David G. MacManus[2], Eric Garnier[3]

ABSTRACT

Flow control devices are used within complex intakes to reduce the flow distortion which can adversely impact the stability and performance of embedded engines. There is a need to assess the capability of modern computational methods such as detached eddy based models to compute the unsteady flowfield and to evaluate the potential benefits of flow control devices on the unsteady distortion. This paper investigates the unsteady flowfield for an S-duct using Zonal Detached Eddy Simulations (ZDES) with passive flow control devices modelled with an overlapping Chimera grid method. The ability of ZDES to evaluate the impact of passive flow control devices on the unsteady flow distortion was assessed. The computed unsteady flowfield at the Aerodynamic Interface Plane was compared with experimental data based on total pressure and velocity field measurements. For the baseline configuration, the ZDES model has proven to be able to simulate the unsteady flowfield at the AIP, to provide the time averaged and fluctuating levels of swirl distortion within 1% and 13% respectively of the measurements. The strong impact of the flow control devices on the AIP flowfield was also captured by the ZDES. The overall increase of pressure ratio (PR) at the AIP due to the flow control devices was predicted with less than 1% error. The 65% reduction in swirl distortion fluctuation when the flow control devices are used was predicted within less than 8% error by the ZDES compared with S-PIV measurements. Overall it was determined that the ZDES method is able to simulate the unsteady flow and distortion characteristics for both the baseline reference configuration as well as the case with flow control.

Keywords: *S-duct intake, vortex generators, unsteady flow distortion, zonal detached eddy simulation, stereo-particle image velocimetry*

Nomenclature

A	=	S-duct cross section area, m^2
Cp	=	Static pressure coefficient defined as $Cp = \frac{p_s - p_{s,ref}}{1/2\rho V_{ref}^2}$
D	=	S-duct cross section diameter, m
$DC60$	=	60˚ sector distortion coefficient
f_d	=	DDES shielding function
H	=	S-duct centreline offset, m
h_{vg}	=	Vortex generators height, m
L	=	S-duct axial length, m

[1] Univ. Lille, CNRS, ONERA, Arts et Metiers Institute of Technology, Centrale Lille, UMR 9014 – LMFL – Laboratoire de Mécanique des Fluides de Lille – Kampé de Fériet, F-59000 Lille, France
[2] School of Aerospace, Transport and Manufacturing, Cranfield University, MK43 0AL, UK
[3] DAAA, ONERA, University Paris Saclay, F-92190 Meudon – France

M = Mach number

P_0 = Total pressure, Pa

p_s = Static pressure, Pa

PDF = Probability Density Function

PR = Total Pressure ratio, $\langle\overline{P_0}\rangle/P_{0,ref}$ at the AIP

R_c = Curvature radius of the S-duct centreline arcs, m

Re_D = Reynolds number based on the inlet diameter

SD = Swirl Directivity based on the SAE definition (Society of Automotive Engineers, 2007)

SI = Swirl Intensity based on the SAE definition (Society of Automotive Engineers, 2007), (°)

SP = Swirl Pairs based on the SAE definition (Society of Automotive Engineers, 2007), rev^{-1}

s = Curvilinear coordinate along the S-duct centreline, m

TKE = Resolved turbulent kinetic energy, m^2/s^2

V_s = Streamwise velocity normal to the local cross section perpendicular to the S-duct centreline, m/s

V_θ = Circumferential velocity for an S-duct cross section, m/s

y^+ = First cell size in the direction normal to the wall, m

Greek symbol

α = Swirl angle (°) defined as $\tan^{-1}\left(\frac{V_\theta}{V_s}\right)$

β_s = Vortex generators toe angle (°)

Δ_{max} = Original sub-grid length scale from Spalart et al. (2006)

Δ_ω = Modified sub-grid length scale from (Deck, 2011)

δ = Boundary layer thickness (m)

θ_s = Circumferential extent in which the VG is placed (°)

μ_t = Eddy viscosity $(Pa.s^{-1})$

σ = Fluctuating component based on the standard deviation

τ_c = S-duct convective time, L_s/w_{ref}

ϕ = Azimuthal angle (°)

$||\omega||$ = Vorticity magnitude, s^{-1}

Operators

$\langle\cdot\rangle$ = time averaged

$\bar{\cdot}$ = area weighted averaged

$|.|$ = absolute value

$std(.)$ = Standard deviation

Subscripts

AIP = Aerodynamic Interface Plane ($0.5D_{in}$ downstream the S-duct outlet plane)

in = S-duct inlet plane

out = S-duct outlet plane

ref = Reference plane

1. Introduction

Embedded propulsion systems are sometimes used in the aircraft industry and are generally associated with complex aero-engine intakes. Fully or partially integrated propulsion systems are used for their potential overall benefit with possible reductions in drag, noise and installation length (Cummings et al., 2018; Florea et al., 2015; Ochs et al., 2016) and are expected to play a major role in the next generation of aircraft (Giuliani and Chen, 2016; Liebeck, 2004). However, S-shaped intake diffusers are susceptible to high levels of flow unsteadiness and distortion (Gil-Prieto et al., 2017a, 2017b). This is typically driven by secondary flows and local flow separations that arise through the duct due to curvature and diffusive properties of the intake (Society of Automotive Engineers, 2017). As a result, complex total pressure and swirl distortion fields, with large unsteady perturbations are presented to the first stage of the compression system at the Aerodynamic Interface Plane (AIP) (Gil-Prieto et al., 2019; Tanguy et al., 2018).

The flow distortion causes a loss in compressor efficiency which reduces the performance of the engine (Society of Automotive Engineers, 2017). The convection of the distortion through the different stages of the compressor can also adversely affect the operability of the propulsion system and promotes the surge of the engine which could compromise the whole integrity of the aircraft (Greitzer, 1980; Stenning, 1980). The use of complex intakes significantly raises the unsteadiness of the flowfield and is responsible for the presence of peak distortion events (Tanguy et al., 2018). These events are generally associated with high levels of swirl which promote the compressor instabilities and can lead to unanticipated reduction in engine surge margin (Jacocks and Kneile, 1975; Society of Automotive Engineers, 2017).

Historically, flow control devices were used to improve the flowfield structure as they can limit the development of secondary flows within complex intakes. Flow control can take the form of passive, active or hybrid. However, the impact of flow control on the unsteady distortion based on time dependent methods is not widely investigated within the literature (Wojewodka et al., 2018). A number of previous studies have investigated the use of passive flow control to reduce the steady distortion at the AIP for circular intake ducts (Anderson and Gibb, 1993; Delot et al., 2011; Owens et al., 2006; Reichert and Wendt, 1996). Passive flow control devices generally take the form of co-rotating vortex generators (VGs) placed within the intake to modify the secondary flows and prevent flow separation inside the duct. However, the use of flow control devices can also generate significant levels of swirl and be associated with multiple loss regions at the AIP (Reichert and Wendt, 1996). Mainly two different approaches can be identified from previous studies within the literature to improve the aerodynamics of S-ducts with vortex generators. The first approach is to use a relatively small number (between 2 and 10) of relatively tall VGs ($h_{vg}/\delta_{in} \geq 1$). In this case, the use of VGs showed a better ability to counter act the secondary flows however, it also showed a detrimental decrease of the pressure ratio (PR) at the AIP. The second approach uses a greater number of VG (from 10 to 22) with submerged vortex generator ($h_{vg}/\delta_{in} < 1$). Small VGs give a better pressure recovery than tall VGs, however a greater number of VGs spread circumferentially is required to fully withstand the natural secondary flows.

Tanguy et al. (2017) applied stereoscopic particle image velocimetry (S-PIV) to measure the velocity field at the outlet of the S-duct investigated in the present work with passive flow control devices. The synchronous high spatial resolution measurements quantified for the first time the impact of vortex generators on the unsteady swirl distortion at the AIP. The addition of vortex generators upstream of the S-duct first bend significantly changed the flow topology with a reduction in pressure loss up to 30% and an improvement of the swirl based distortion up to 50%. The analysis of the unsteady distortion at the AIP also demonstrated the strong impact of the vortex generators on the flowfield.

Computational Fluid Dynamics (CFD) is used to support the development of complex intakes. Today, steady state computations represent a valuable tool for the optimization of intake design with (Jirásek, 2006; Yi et al., 2012) and without (Edefur and Tormalm, 2018; Jirasek et al., 2018) flow control devices at a relatively low computational cost. However, these models have proven to be inadequate for the prediction of massively separated flows fields where the dynamics of large scale turbulent structures play a central role in the flow behaviour. Furthermore, steady state models are sensitive to the turbulence model used and often fail to match simultaneously the level of distortion and pressure losses at the AIP (Delot and Scharnhorst, 2015). While Reynolds Averaged Navier-Stokes (RANS) methods are widely used for the computation of steady solutions for aero-engine intakes, the use of methods to predict the unsteady distortion at the Aerodynamic Interface Plane (AIP) only received attention in the last decade. Unsteady CFD solutions can be computed at a viable cost by the use of hybrid RANS/LES models which resolve the turbulence within the separated and mixing flow regions. These models are efficient and accurate for the simulation of external flowfield and mixing layer (Deck, 2011; Spalart et al., 2006). However, hybrid RANS/LES models have shown some limitations for flows where the switch from modelled-to-resolved turbulence is ambiguous (Spalart, 2009) and strongly depend on the local grid refinement.

Berens et al. (2014) presented the result from several organisations which performed hybrid RANS/LES calculations of the RAE M2129 S-duct (H/L = 0.30, A_{out}/A_{in} = 1.42) (Figure 1a) to test the capability of hybrid models to predict the level of unsteadiness at the AIP. A total of 13×10^6 cells was used for the mesh of the S-duct unsteady simulation with an inlet Mach number of 0.66 ($Re_{D_{in}} = 1.6 \times 10^6$). This intake, which has a relatively low offset (H/L = 0.30), had total pressure loss regions in the lower section of the AIP associated with a centreline separation and secondary flows. The Detached Eddy Simulation (DES) model was used to identify the maximum level of unsteady total pressure distortion at the AIP which was twice the time averaged value (Berens et al., 2014). However, the mean circumferential distortion obtained for the DES solution was 66% higher than the experimental value. Furthermore, a delay in the development of instabilities within the region of resolved turbulence showed the limitation of that DES model.

MacManus et al. (2017) numerically investigated the unsteady flow for two S-duct configurations with the Delayed Detached Eddy Simulation model (DDES) using the $k-\omega\ SST$ turbulence model for the closure of the RANS equations. These two configurations were previously investigated experimentally by Delot et al. (2011) and Garnier (2015) at ONERA. MacManus et al. (2017) used a mesh of 5×10^6 cells for two AIP Mach numbers (M_{AIP}) of 0.18 and 0.36. The unsteady simulation was used to assess the flowfield at the AIP and compared with the experimental data based on conventional unsteady total pressure measurements from Delot et al. (2011) and Garnier (2015). The study showed that for both ducts, high levels of total pressure and swirl fluctuations were present at the AIP with local instantaneous swirl values as large as twice the mean value. The spectral signature of the total pressure flowfield at the AIP demonstrated the presence of correlated structures previously identified by Delot et al. (2011) and Garnier (2015) experimentally. The Proper Orthogonal Decomposition (POD) of the total pressure flowfield highlighted those coherent structures corresponding to a lateral and vertical oscillation of the main total pressure loss region at the AIP.

Gil-Prieto et al. (2017b) investigated the unsteady flowfield for an S-duct intake (A_{out}/A_{in}=1.52, H/L = 0.49, L/D_{in} = 4.95) with DDES at an inlet Mach number of 0.27. The multi-plane POD analysis of the velocity data at both the AIP and symmetry plane of the duct identified the origin and streamwise characteristics of the most energetic flow mode. The CFD solution confirmed that the vertical perturbation mode previously highlighted by MacManus et al. (2017) was promoted by the shedding of the span wise vortices from the shear layer formed by the separation region within the S-duct. The study also revealed that lateral oscillation of the main loss region at the AIP previously identified by MacManus et al. (2017) was associated with the alternate shedding of contra-clockwise and clockwise streamwise vortices that originate from the

downstream part of the separation region (Gil-Prieto et al., 2017b). This flow mode referred to as swirl switching was also previously found by Hellström et al. (2013) and Kalpakli Vester et al. (2015) during the study of the exit flow from bent pipe investigations.

The unsteady flowfield for a serpentine S-duct (H/L = 0.22) has been investigated by Delot et al. (2014) with several DES models. Compared with more canonical S-ducts, serpentine S-ducts are intakes made of three changes of centreline curvature and typically associated with a non-circular inlet section that can develop higher losses in total pressure at the AIP due to the separation region at the second bend. Furthermore, the secondary flows developed by the first bend of the S-duct result in additional loss regions at the AIP. The computation performed by ONERA (Delot et al., 2014) used a mesh of 44×10^6 cells with a time step of $2.5 \times 10^{-7} s$. The Zonal Detached Eddy Simulation (ZDES) model was used to allocate the use of URANS for regions where the serpentine duct boundary layer was attached and the LES model for separated and vortical flows. The distribution of the wall static pressure along the serpentine duct indicated that the ZDES computation over predicted levels of Cp within the separation region on the bottom surface by a factor of 2 compared with experimental data. As a result, the level of circumferential distortion (DC60) at the AIP was 10% higher than the experimental one. Nevertheless, the total pressure ratio (PR) at the AIP was predicted within less than 1% error compared with the experiment and proved to be more accurate than the RANS solution (Delot et al., 2014).

Connolly et al. (2018) used Improved Delayed Detached Eddy Simulations (IDDES) (Shur et al., 2008) to estimate the unsteady flow field for an S-duct with a rectangular cross section with a high aspect ratio. The S-duct configuration from Gil-Prieto et al. (2017b) was also reproduced by Connolly et al. (2018) in order to validate the IDDES model which demonstrated similar flow mechanisms as the rectangular S-duct. Overall, the results showed the presence of Dean Vortices similar to those in circular section ducts, however these are confined to regions near the lateral end walls. The main separation is also reduced due to the high aspect ratio of the cross section. Connolly et al. (2022) pursue their work into simulating an Inertial Particle Separator duct with a rectangular cross section in order to identify potential region of flow separation and calculate the efficiency of the bifurcating duct. The results were compared with experimental data and provided a good agreement for mean and fluctuating flow field near the bifurcating section.

Based on the literature, the investigation of passive flow control devices within S-duct intakes with unsteady simulations has received little attention. An attempt to evaluate the effect of passive flow control devices for an S-duct intake ($\mathrm{H/D_{AIP}}$ = 1.04, $\mathrm{A_{out}/A_{in}}$ = 1.07) was made by Mace et al. (2012). The S-duct geometry was representative of an intake for a Blended Wing Body (BWB) with an embedded engine. As a result, the inlet cross-section was semi-circular compared with fully circular for the geometry investigated in this study. A configuration with 10 vortex generators previously investigated experimentally by McMillan et al. (2011) was placed at a distance of 0.4 D_{AIP} from the S-duct inlet. The vortex generators had a height of $0.10D_{AIP}$ and the total number of cells for the unstructured grid was 46×10^6. The unsteady computation was performed with the DDES-SA model proposed by Spalart et al. (2006). The operating condition for the simulation was based on an AIP Mach number of 0.63. Overall, Mace et al. (2012) demonstrated the feasibility of using a hybrid RANS/LES method to predict the unsteady total pressure distortion at the AIP when flow control devices are used. The total pressure fluctuation levels at the AIP were found to be higher than with the experimental data. Unfortunately, the total time of simulation was not sufficient to provided fully statistically converged results. However, comparable frequency spectrums were found when comparing individual pressure measurements from the experiment with the CFD solution. Mace et al. (2012) concluded that hybrid RANS/LES models required improvement in the blending function along with low dissipation discretization scheme to properly reproduce the unsteady distortion for S-duct intake with flow control devices. Burrow et al. (2019) also performed computations on the BWB duct to investigate the use of active flow control

to influence the separated flow generated by a "trap vorticity" recessed surface. The use of DDES-SA simulations, necessary to resolve the separated flow within the S-duct, permits the identification of the mechanism that reduced the flow distortion at the AIP due to the hybrid flow control method.

Noetling et al. (2015) used Lattice-Boltzmann Method (LBM) to compute the S-duct flow field with and without the flow control devices from Delot and Scharnhorst (2015). The LBM successfully reproduced the effect of the vortex generators at the AIP and was able to predict the time averaged total pressure ratio within less than 0.3% compared with the ONERA experimental data. Unfortunately, while the instantaneous flow structured within the S-duct could be identified, the unsteady statistics at the AIP were not presented.

Lakebrink and Mani (2018) performed a DDES-SA (Spalart et al., 2006) simulation of a serpentine duct with and without active flow control devices. The unstructured mesh size was 364×10^6 cells and the simulation was carried for inlet Mach numbers of 0.56, 0.69 and 0.77. Lakebrink and Mani (2018) investigated the sensitivity of the near wall simulation by modifying the coefficients from the blending function f_d developed by Spalart et al. (2006). It was found that the original version of the blending function provided the best agreement with the experimental data in terms of flow velocity fluctuations and total pressure loss. However, Lakebrink and Mani (2018) demonstrated that for refined grids, the DDES-SA model tends to be sensitive to the coefficient used by the blending function. This example highlighted the need for robust shielding functions for hybrid RANS/LES models when small scale perturbations are present.

Thompson and Komives (2019) also investigated the unsteady flow field of the same serpentine S-duct without flow control. However, a Wall Modelled LES (WMLES) model, combined with a higher order numerical methods using a structured grid, were used in order to reduce the computational cost of the simulation. The results obtained were comparable to those from Lakebrink and Mani (2018) as long as a 4^{th} order spatial discretisation scheme was used.

The serpentine duct was also investigated by Burrow et al. (2021). The results of the DDES-SA calculation were compared with an extensive data set based on total pressure measurements at the AIP, pressure sensitive paint and oil-flow visualisation within the intake. The use of active flow control after the second bend of the duct strongly changed the flow topology inducing large scale structures with vorticity cells rotating in the opposite sense to the baseline flow. As a result, the separation at the second bend is reduced and the formation of streamwise twin vortices on the upper part of the AIP is modified into two distinct regions of vorticity similarly as Tanguy et al. (2017). The total pressure distortion could be reduced up to 60% at the AIP due to the use of the actuated jets. Although, the intake investigated by Burrow et al. (2021) and Tanguy et al. (2017) are significantly different, the flow mechanism that drives the secondary flows remains similar.

Therefore, hydrid RANS/LES models are now commonly used to assess the unsteady flow field of complex intakes in order to assess their performance at an affordable computational cost compared with a full LES calculation. However, these models can suffer from limitations mainly due to the shielding of the boundary layer and the slow development of the shear layer instabilities which can strongly impact the flow field at the AIP. There is also a need to assess if unsteady CFD models can simulate the unsteady flowfield within complex intakes with enough fidelity to reproduce the unsteady swirl and pressure distortions at the AIP which are liable to strongly impact the performance and stability of the compressor system. The validation of unsteady CFD methods for complex intakes requires synchronous measurements with a high spatial resolution to establish whether hybrid models can capture not only the pressure and velocity main fluctuation levels but also the correct flow frequencies and coherent structures. However, this cannot be provided with conventional AIP flow measurements techniques based on intrusive total pressure rakes. Finally, the capacity of hybrid RANS/LES models to reproduce the effects of passive flow control devices on the unsteady swirl distortion at the AIP has not been previously investigated.

The aim of the present work is to investigate the capability of a hybrid RANS/LES model to simulate the unsteady flow distortion metrics with and without flow control devices for an S-duct intake. The work follows on the study of Mace et al. (2012) and Burrow et al. (2021) by investigating the unsteady flow field of a canonical S-duct diffuser, and the impact of vortex generators over the AIP flow field. The novelty of this work mainly lies into the computational method used and the analysis of the AIP unsteady flow field. The Zonal Detached Eddy Simulation model is used to assess the unsteady flow field within the intake and at the AIP. The ZDES model is used with a local vorticity based sub-grid length-scale Δ_ω, which is known to reduce the dissipation within separated flows and promote the development of flow unsteadiness with a rapid switch from RANS to LES model (Deck, 2011) compared with classical DDES models. The recent work simulating the impact of flow control on the unsteady flow field within S-ducts are based on active devices. The present study investigates the impact of passive flow control on a high offset S-duct which develops significant levels of distortions at the AIP and provides a challenging configuration for hybrid RANS/LES calculation with a different flow physics to reproduce. Finally, the unsteady swirl distortion at the AIP is quantified based on time dependent CFD solutions and dedicated experimental data. Furthermore, the flow field is validated with the use of high spatial resolution 3C S-PIV measurements at the AIP, which provide a rich velocity data set that also permits to compute the unsteady swirl flow distortion metric.

2. Experimental test case

2.1. S-duct geometry and flow control configurations

The S-duct intake (Figure 1a) used for this study was previously investigated experimentally (Garnier, 2015; Gil-Prieto et al., 2017a; Tanguy et al., 2017). The centreline is made of two symmetrical arcs with a radius R_c/D_{in} = 3.125 and a maximum arc angle θ_C = 52.55°. The S-duct has a circular section with a diffusion area $A_{out}/A_{in} = 1.52$ with an outlet diameter $D_{out} = 150mm$ (Figure 1a). The length of the S-duct (L/D_{in}) and the offset to length ratio (H/L) are equal to 4.95 and 2.44 respectively. The current S-duct geometry previously investigated by Garnier (2015) was derived from the intake investigated by Wellborn and Okiishi (1993) with similar geometrical properties with the exception of H/L which was equal to 0.49. The Aerodynamic Interface Plane (AIP) is located at a distance of $0.5D_{in}$ from the S-duct outlet.

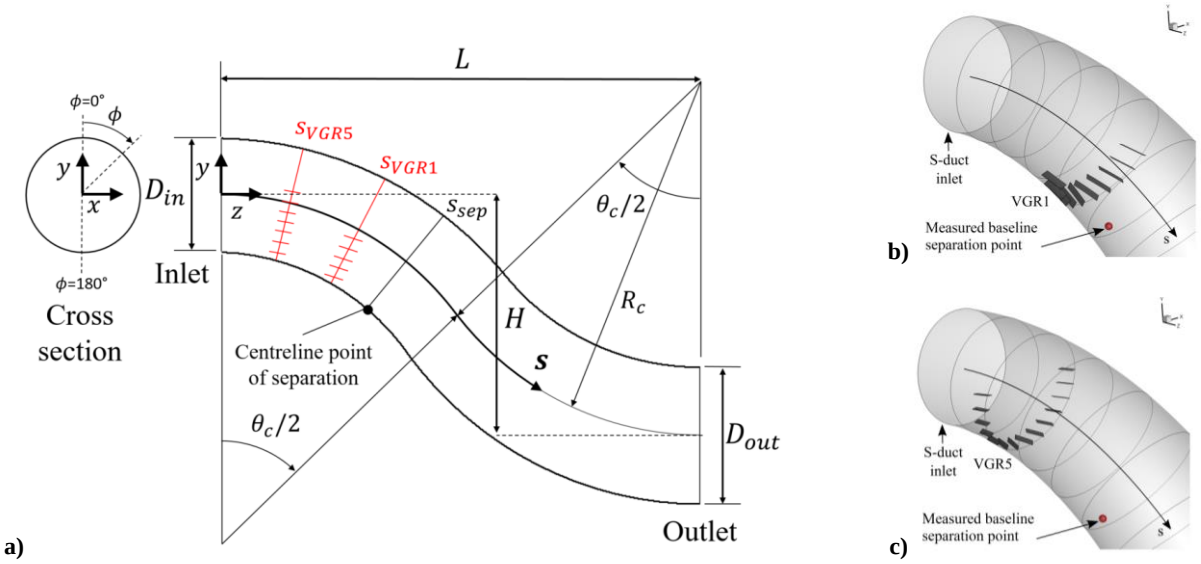

Figure 1 S-duct geometry definition (a) and illustration of the vortex generator configurations VGR1 (b) and VGR5 (c)

This paper investigates two passive flow control devices represented by rectangular vortex generators (VG). Both configurations are derived from the previous work of Tanguy et al. (2017) which examined the sensitivity of the VG axial position, the VG height and the number of VG on the flowfield at the AIP. The configuration VGR1 lies in the first category of vortex generators identified within the literature. The VGs have a height (h_{vg}) of $0.057D_{in}$ $(1.27\delta_{ref})$ and are placed close to the measured separation point corresponding to the baseline configuration ($s_{sep} = 1.97D_{in}$). The vortex generators are placed along the centreline distance $s = 1.55D_{in}$ (Figure 1a). The configuration VGR1 is made of 10 vortex generators distributed over a circumferential extent of $\theta_{vg} = 67.5°$ (Figure 1b). The aspect ratio and toe angle are $L_{vg} = 4h_{vg}$ and $\beta_{vg} = 16°$. This configuration was also selected in order to provide a test case from Tanguy et al. (2017) which was close to the work of Delot and Scharnhost (2015) and Mace and al. (2012). The configuration VGR5 is made of a greater number of VGs with lower height than the inlet boundary layer ($h_{vg}/\delta_{in} < 1$). Based on the experimental results of Tanguy et al. (2017), the characteristics of VGR5 should provide the best improvement of the flow field in terms of swirl and total pressure distortion reduction at the AIP. The configuration VGR5 is made of 14 vortex generators (Figure 1c) placed over a circumferential extent θ_{vg} of 97.5° at the streamwise location $s = 0.74D_{in}$ (Figure 1a). The height of the VGs (h_{vg}) are $0.041D_{in}$ $(0.91\delta_{ref})$, the aspect ratio (L_{vg}/h_{vg}) and toe angle (β_{vg}) are also respectively 4° and 16° as VGR1. The heights (h_{vg}) of VGR1 and VGR5 are also compared with the bottom surface boundary layer obtained with the baseline CFD solution for their respective location (δ_{loc}). For VGR1 and VGR5, h_{vg}/δ_{loc} is 0.55 and 0.56 respectively which indicates that both configurations are submerged vortex generators relative to the expected local boundary layer thickness. Within the literature, it is typical to report VG size relative to reference inlet plane (h_{vg}/δ_{ref}). However, it is of interest to note that there can be notable variation of the local boundary layer height within these complex ducts, which can change the relative size of the VG to the local boundary layer thickness, as in this example.

2.2. Experimental facility and measurements techniques

The experimental work was performed with a transonic suck-down intake rig. The facility can accommodate several measurements techniques to assess the flowfield at the AIP such as total pressure rakes or Stereo Particle Image Velocimetry. More details of the experimental facility can be found in the work of Zachos et al. (2016) and Tanguy et al. (2017). The S-duct operating condition was defined in terms of the centreline reference Mach number (M_{ref}). The incoming boundary layer profile was measured at the reference plane located $1.5D_{in}$ upstream of the S-duct inlet with a flattened Pitot probe. The reference Mach number investigated for this paper was 0.60 with a typical Reynolds number based on the inlet diameter of $Re_D = 1.42 \times 10^6$ at a nominal atmospheric pressure and temperature of about 100 kPa and 288 K, respectively. Based on the calibration, transducer uncertainty and stochastic terms, the estimated uncertainty on M_{ref} was 0.007.

The static and total pressure flowfield was measured at different locations within the rig. At the AIP, a bespoke cylindrical working section which can rotate along the longitudinal axis was used to support up to 6 total pressure rakes. The steady total pressure measurements at the AIP were acquired with total pressure rakes made of ten Pitot tubes with an outer tip diameter of 1.1 mm. The spatial resolution was doubled by radially translating the rakes. Typically 1440 steady total pressure measurement points are taken at the AIP with a radial resolution of approximately 3.74 mm and circumferential resolution of 5°. The steady pressure measurements were acquired with 50kPa-range low-bandwidth pressure transducers. A sampling rate of 900Hz and a sample number of 10000 were used to evaluate the time-averaged total pressure distributions at the AIP. The uncertainty of the pressure ratio $PR = \langle \overline{P_0} \rangle / P_{0,ref}$ at the AIP based on the error

propagation of the total pressure measurement including both deterministic and stochastic elements is 0.003 for $M_{ref} = 0.6$.

The steady wall static pressure along the S-duct was also measured with 45 static pressure ports pneumatically connected with a Scanivalve MPS4264 pressure scanner. The static pressures were acquired at a frequency of 500Hz for 5s. The measurement points were distributed along the streamwise direction at three azimuthal positions at $\phi = 10°, 90°$ and $170°$ where $\phi = 0°$ is the top dead centre (Figure 1a). The unsteady total pressure at the AIP was measured with two high-sensitivity ultra-miniature pressure transducers XCS-062-5PSID placed within two bespoke Pitot probe mounts. The unsteady probe has an outer tip diameter of 2.95 mm ($0.017D_{AIP}$). In total the AIP flowfield was assessed with 112 unsteady measurement points on a radial and azimuthal spacing of 10 mm and 12.5°, respectively. The unsteady pressure measurements were acquired at a sampling rate of 20 kHz with a sample number of 262144 (2^{18}). The output signal was filtered with a 5 kHz low pass filter.

Stereo Particle Image Velocimetry (S-PIV) was used to measure three velocity components snapshots at the AIP. Two TSI PowerView Plus 8MP rectangular sensors were used with AF 1.8/D Nikkor lenses with a focal length of 50 mm. The two CCD cameras were mounted symmetrically from each side of the rig at an angle of approximately 45°. The laser was a dual cavity pulsed Nd: YAG laser with a wave length of 532 nm and a maximum power of 200mJ per pulse. The light sheet had an estimated thickness of 1.5 mm at the AIP. The repetition rate used to acquire the velocity field snapshots was 3.5 Hz. Therefore, the S-PIV measurements do not provide the detailed temporal component of the flowfield. However, the measurement enabled a statistical assessment of the flowfield and the distortion metrics.

The seeding was Diethylhexyl sebacate (DEHS) particles with an estimated diameter of 1 μm. The use of 8M pixels CCD cameras also provided particle image diameters about 4 to 6 pixels which was enough to prevent peak locking (Raffel et al., 2007). The maximum frequency response of the particle estimated with the method proposed by Melling (1997) was 3 kHz which is about 3 times the maximum range of frequency observed at the AIP.

The magnification factor and the viewing direction of each camera are found by a calibration procedure using a spatial target plate marked by a rectangular grid of uniformly distributed dots at 10mm spacing. A 3-plane axial traverse method with an inter-plane spacing along the longitudinal axis of 0.375 mm was used to determine the spatial calibration factors. The grid mapping is determined with 3rd order polynomials for the lateral and vertical components and a 2nd order polynomial for the longitudinal displacement. The potential error introduced by the misalignment between the laser light sheet and the calibration target was systematically mitigated with a disparity correction process (Wieneke, 2005). The disparity map was computed over 100 snapshots for each data set with the minimum intensity background subtracted. The calibration polynomials then are corrected to minimise the disparity through an iteration process. The resulting error in pixel displacement associated with the disparity is $\sigma_{disp} = 0.006$px.

The PIV images pre-processing was used with a background subtraction method to remove the visual impact of seeding accumulation laser light reflections and static features in the images. A recursive Nyquist grid with 50% overlaps was applied as a grid engine for the cross-correlation using a Fast Fourier Transform (FFT). The first pass was executed over a 64 x 64 pixels interrogation area with a 5 x 5 validation pass. The second pass decreases the grid size to 32 x 32 with 50% overlap window for the cross correlation. About 8000 velocity vectors were calculated for the AIP with a spatial resolution approximately equal to 1.5 mm ($0.01D_{AIP}$).The number of S-PIV snapshot used for this analysis was determined with a statistical convergence study based on velocity and swirl distortion fluctuations at the AIP. The standard deviations of the area-weighted average velocity and swirl distortion descriptors (SI, SP and SD) were converged within 1% of the value calculated over 1500 snapshots for data set of more than 700 and 800 respectively. Therefore, a total number of 1000

snapshots were used for each case which was considered sufficient to assess the dynamic flowfield at the AIP at $M_{ref} = 0.60$.

The overall uncertainty of the S-PIV measurements was assessed using the method proposed by Charonko and Vlachos (2013). This method estimates the PIV uncertainty of the pixel displacement based on the signal to noise ratio (SNR) obtained in the cross correlation process (Eq. 1). The method is based on the analysis of synthetic images of reference flow fields obtained from analytical solutions and DNS results. The SNR level is defined as the ratio between the first and second correlation peaks obtained in the cross correlation of the PIV windows. The method should account for all the sources of uncertainty associated with the correlation process such as particle size, background noise, velocity gradients across the interrogation wind and out-of-plane motion.

$$\epsilon^2_{||u_p||} = \left(M\, e^{-\frac{1}{2}\left(\frac{SNR-1}{s}\right)^2} \right)^2 + \left(A \times SNR^B\right)^2 + C^2 \quad (1)$$

In Eq. 1, the constant M, s, A, B and C have been empirically determined for a Fourier-based cross-correlation engine and phrase correlation engine. The uncertainty ϵ_{u_p} represents the uncertainty of the modulus of the displacement vector. Therefore, the 95% coverage uncertainty for a single component of the in-plane velocity is obtained with Eq. 2. For this work, the S-PIV process uses an FTT cross-correlation engine. The constants prescribed by Charonko and Vlachos (2013) are then M = 13.1, s=0.226, B=-1 and C=0.08 for Eq. 1.

$$\epsilon_{u_{p95}} = 1.96 \frac{\epsilon_{||u_p||}}{\sqrt{2}} \quad (2)$$

It was recognised that for a FFT based cross-correlation engine, the method had the tendency to overestimate the true error in pixel displacement. The standard deviation evaluated by the method gives a coverage of 81% for the error obtained from the synthetic images. This is above the 68% coverage attributed to the standard deviation of the true error. Therefore, the method proposed by Charonko and Vlachos (2013) provides a conservative assessment of the PIV uncertainty.

The time averaged individual velocity component uncertainty in pixel displacement $\epsilon_{u_{p95}}$ has been computed for a representative data set of 1000 snapshots at the AIP. The face averaged uncertainty for the port and starboard camera are 0.16px and 0.13px respectively. The uncertainty of the in-plane velocity $\left(\epsilon_{V2d_{95}}\right)$ component can be converted to m.s^{-1} with Eq. 3.

$$\epsilon_{V2d_{95}} = \epsilon_{u_{p95}} \frac{L_{px}}{\Delta_t} \quad (3)$$

$$\epsilon_{V3D_{95}} = \frac{\epsilon_{V2D_{95}}}{\sqrt{2}} \quad (4)$$

Within Eq. 3, L_{px} is the physical size of the pixel obtained from the camera magnification factor, sensor resolution and physical size of a single pixel, and Δ_t is the time delay between two laser pulses. The uncertainty on the reconstructed velocity components $\epsilon_{V3D_{95}}$ is obtained by propagating the error in $\epsilon_{V2d_{95}}$ through the relationship used for a viewing camera angle of 45°. As a result, the overall uncertainty $\epsilon_{V3D_{95}}$ estimated from the method of Charonko and Vlachos (2013) was 2.5 m/s, which is 2% of the time averaged out-of-plane velocity at the AIP. The uncertainty of the swirl angle (α) at the AIP derived from the out-of-plane velocity (w_{AIP}) and the circumferential velocity (V_θ) is obtained by propagation of the error $\epsilon_{V3D_{95}}$ assuming $\epsilon_{w_{AIP}} = \epsilon_{V_\theta} = \epsilon_{V3D_{95}}$. The uncertainty on the swirl angle measurement at the AIP is 1.2°. The uncertainty of the mean swirl intensity $\langle SI \rangle$ descriptor at the AIP is assessed with the central limit theorem for an AIP discretisation of 9 rings and 72 rakes which result in $\epsilon_{\langle SI \rangle} = 0.1°$ which is 1.2% the baseline mean swirl intensity.

3. Numerical methodology

The CFD investigation was performed using the hybrid RANS/LES method Zonal Detached Eddy Simulation (ZDES) (Deck, 2011). The simulations were performed using the CFD code elsA developed by ONERA (Mayeur et al., 2016). This code solves the compressible Navier-Stokes equations in their integral forms over a multi block structured grid. It uses a finite volume method which consists of integrating the flow solution using a cell centred method.

3.1. Domain and boundary conditions

The computational domain includes the 3D S-duct intake with appropriate upstream and downstream sections (Figure 2). A multi block structured grid was used for the baseline duct. The domain central region is made of an H-topology grid connected with an O-topology grid. The grid spacing is made to satisfy a recommended grid wall unit for ZDES applications based on previous research with separated flow (Le Pape et al., 2013; Richez et al., 2015). The height of the first cells adjacent to the walls varied from 2.7 µm for the upstream section up to 4.3 µm for the downstream section of the domain which satisfies the criterion $\Delta y^+ < 1$. The azimuthal wall unit $r\Delta\theta^+$ does not exceed 400 with $r\Delta\theta < 1$mm. The grid spacing in the streamwise direction within the S-duct varies from 1.2 to 0.8 mm which provides a maximum Δz^+ of 450 near the duct accelerated regions. However, $\Delta z^+$is less than 300 for most the S-duct. Downstream of the S-duct exit, the longitudinal cells size was maintained to 1.25mm for a section of $1.25D_{in}$ long. The central region of the S-duct is made of homogenous cells in the radial and azimuthal directions ($\Delta r = r\Delta\theta < 0.5$ mm). A total of 54×10^6 nodes were used for the baseline grid.

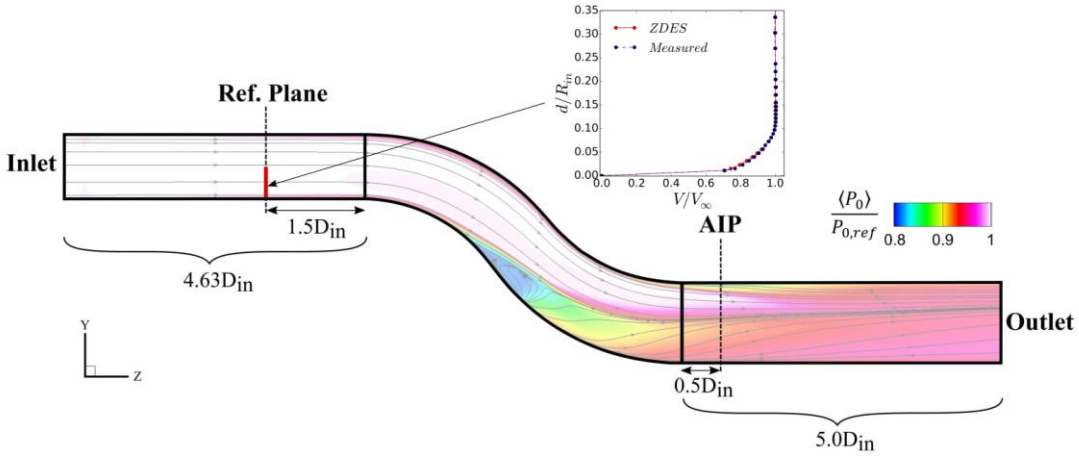

Figure 2 Illustration of the CFD domain with the baseline configuration time-averaged flow solution at the symmetry plane and boundary layer at the reference plane

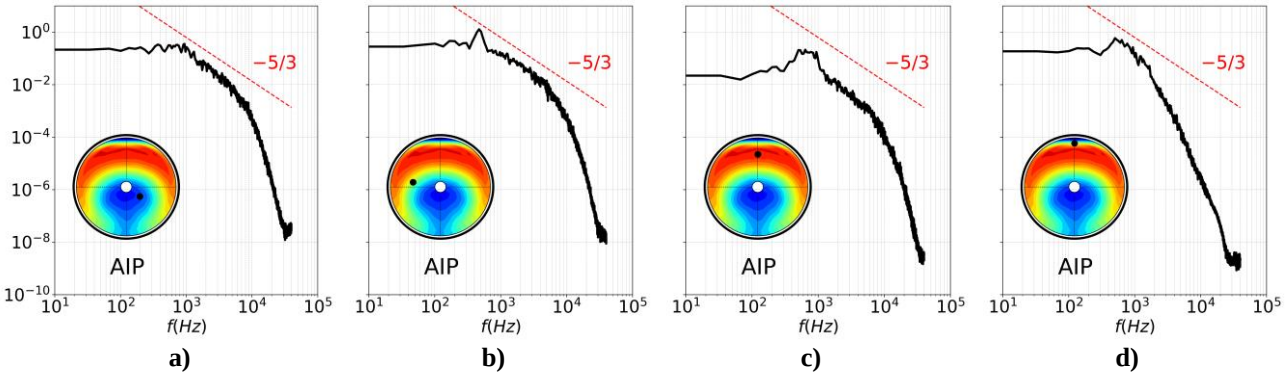

Figure 3 Power Spectral Density for the streamwise velocity at the AIP for the baseline configuration

The grid was made to provide the sufficient resolution to resolve the high flow unsteadiness of the main loss region at the AIP. For a hybrid RANS/LES simulation, the grid spacing requires that the frequency cut off for the LES region is within the inertial subrange of the turbulence spectrum (Georgiadis et al., 2010). The streamwise velocity spectrum at the AIP shows a LES frequency cut-off between 5 and 10 kHz where the spectrum can no longer be associated with a -5/3 slope coefficient (Figure 3 a, b and c). Therefore, the unsteady simulation resolves most of the turbulent spectrum with a frequency cut off located in the inertial subrange. For the region at the top of the AIP, the flow field is mainly simulated with URANS as the boundary layer is attached. Therefore, the velocity fluctuations are damped by the URANS which lower the energy level at high frequency (Figure 3d).

The length of the upstream duct ($4.63D_{in}$) was tailored to provide a close match of the measured boundary layer profile at the reference plane located $1.5D_{in}$ upstream of the S-duct inlet (Figure 2). The computed boundary layer had a 1% and 7% error for the boundary layer thickness (δ_{ref}) and displacement thickness (δ^*_{ref}), respectively. At the reference plane, the first mesh point along the bottom surface is placed at a y^+ value of 0.3 and 7 nodes are gathered within the linear viscous sub layer of the boundary layer. A uniform total pressure profile is imposed at the inlet of the domain to match the mid-height total pressure measured at the reference plane. The total temperature used for the inlet condition was 296K which corresponds to the typical ambient temperature during an experiment. The static pressure at the outlet of the domain was selected to match the operating reference Mach number measured at the reference plane (M_{ref}). The downstream section is $5D_{in}$ long to prevent any influence of the outlet conditions over the main flowfield.

3.2. Flow control implementation

Two flow control configurations have been simulated in order to identify the flow mechanisms responsible for the distortion reduction at the AIP. The implementation of flow control devices increases the complexity of the grid for a structured mesh as it requires a grid refinement around the devices and in the wake to properly simulate the flowfield. The overset grid method, commonly known as the Chimera method, has been chosen to implement the vortex generators within the domain (Figure 4). Each vortex generator (VG) is represented with an individual grid. The mesh is generated with a dedicated grid generator developed at ONERA (Boniface et al., 2013; Gibertini et al., 2015) and adapted for this application. The VG is defined as a wall boundary condition in a block structured grid. The VGs can be individually positioned inside the S-duct without redefining the pre-existing background grid. This also provides the advantage to locally refine the grid to capture the formation of the trailing vortex. For this application, the mesh of a vortex generator is built as two structured blocks. The bottom surface of the grid is coincident with the local wall surface of the domain. The structured H-type grid is refined in the direction normal to the surface of the duct to maintain a y^+ value of 1. The width and length

of the block are respectively $2.35h_{vg}$ and $18h_{vg}$ with a distance between the trailing edge of the VG and the downstream frontier of the domain equal to $10h_{vg}$. To reduce the mesh complexity and computational cost of the simulation, the VG is modelled as a flat plate with no thickness. The number of nodes per VG grid is 1.4×10^6 which results in a maximum size of 74×10^6 nodes for the mesh including the vortex generator devices. The overset method used in this study is the patch assembly approach (Blanc, 2010). This method provides an automatic patch overlapping grids assembly for the background grid (S-duct) and the patch grid of the new added feature (the vortex generators). The patch assembly method automatically identifies the region of interpolation between the two grids based on the patch grid frontier and is made to optimise the amount of cells blanked in the background grid. The blanking of the background grid suppresses the computation of non-physical flow within the background grid and removes the unnecessary interpolated cells to reduce the computation cost of the interpolation process.

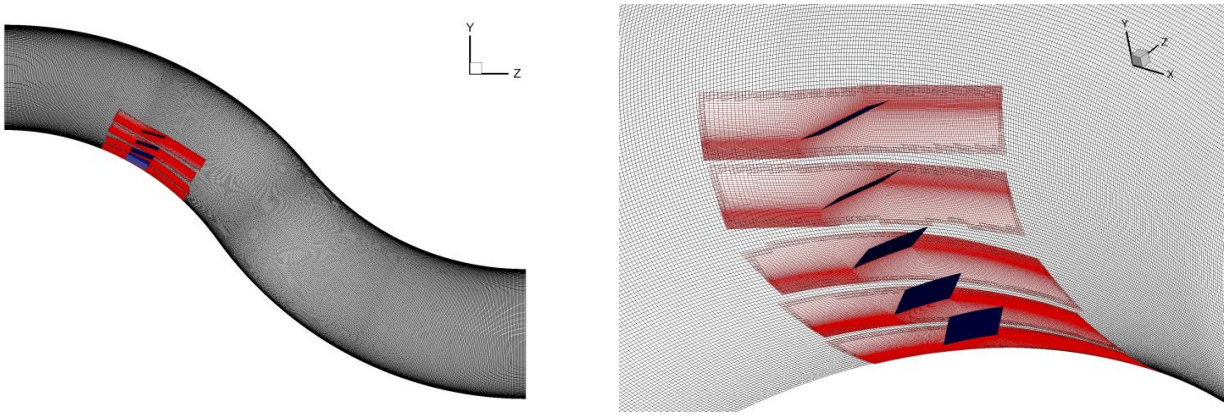

a) **b)**

Figure 4 Representation of the Chimera mesh for VGR1

3.3. Turbulence modelling: Zonal Detached Eddy Simulation

The Zonal Detached Eddy Simulation (ZDES) approach is used to simulate the unsteady flowfield for the S-duct including the flow control devices. Hybrid RANS/LES methods such as the ZDES offer a less expensive computational method compared with full LES but still resolve the majority of the large scale structures within the unsteady flow (Sagaut et al., 2013). However, the use of hybrid methods on complex configurations often leads to ambiguous grid sizes (also called grey-area) where the switch from URANS to LES can happen within the boundary layer (Spalart, 2009) and generates a local loss of eddy viscosity. The low level of velocity fluctuations within the LES part of the boundary layer cannot compensate for the reduction of modelled stress tensor. This phenomenon is called Model Stress Depletion (MSD) and is associated with an under-prediction of the skin friction coefficient and can lead to unphysical separation of the flow referred to as grid induced separation (GIS) (Spalart, 2009). Furthermore, separated flows and mixing layers addressed with hybrid RANS/LES methods can suffer from a delay in the development of instabilities due to the absence of turbulent fluctuations within the URANS regions.

The Zonal Detached Eddy Simulation (ZDES) developed by Deck (2011) was initially proposed to suppress the Model Stress Depletion grid sensitivity and to promote the formation of instabilities once the flow switches from RANS to LES. The initial formulation of the ZDES was developed with the turbulent model Spalart-Allmaras (SA) as for the DES97 (Spalart et al., 1997) and DDES-SA models (Spalart et al., 2006). The activation of the DES content during a simulation is performed with the change of the length scale $\tilde{d}_{ZDES}$ within the turbulent transport equation of the SA model (Eq. 5)

governing the pseudo eddy viscosity variation ($\tilde{\nu}$). Through the development of the model, several modes have been established in order to adapt the length scale $\tilde{d}_{ZDES}$ according to different flow classifications as defined by Deck (2011).

$$\frac{D\tilde{\nu}}{Dt} = c_{b1}(1-f_{t2})\tilde{S}\tilde{\nu} + \frac{1}{\sigma}\left[\nabla.\left((\nu+\tilde{\nu})+\nabla\tilde{\nu}\right)+c_{b2}(\nabla\tilde{\nu})^2\right] - \left[c_{w1}f_w - \frac{c_{b1}}{\kappa^2}f_{t2}\right]\left(\frac{\tilde{\nu}^2}{\tilde{d}_{ZDES}}\right) \quad (5)$$

Based on the previous experimental and numerical research (Gil-Prieto et al., 2017a, 2017b), the main aerodynamic features issued from the investigated S-duct have been identified. For the baseline configuration (i.e. without VGs), the flowfield separates on the lower surface of the duct due to a strong adverse pressure gradient, secondary flows and a diffusion process (Figure 2). The ZDES mode 2 (Deck, 2011) has been selected to simulate the flowfield as the separation point within the S-duct is not known a priori. The length scale $\tilde{d}_{ZDES}$ is defined as $\tilde{d}_{DES}^{II}$ (Eq. 6) is similar to the original DDES-SA formulation of Spalart et al. (2006). The mode 2 provides an automatic switch from URANS to DES based on the blending function f_d (Eq. 7) to differentiate whether a cell is or is not within an attached boundary layer. The variable r_d (Eq. 7) comes from the initial formulation of the SA model which assesses if a cell is located outside ($r_d << 1$), within the logarithm region ($r_d = 1$), or in the near wall region ($r_d > 1$) of the boundary layer. As a result, the shielding function f_d takes the value of 1 within the boundary layer and 0 elsewhere. Therefore, within the boundary layer, $\tilde{d}_{DES}^{II} = d_w$ which triggers the RANS mode while outside the boundary layer $\tilde{d}_{DES}^{II} = C_{DES}\tilde{\Delta}_{DES}^{II}$.

$$\tilde{d}_{DES}^{II} = d_w - f_d max\left(0, d_w - C_{DES}\tilde{\Delta}_{DES}^{II}\right) \quad (6)$$

$$f_d = 1 - \tanh[(8r_d)^3] \; with \; r_d = \frac{\nu_t + \nu}{\sqrt{U_{i,j}U_{i,j}}\kappa^2 d_w^2} \quad (7)$$

The sub-grid length scale $\tilde{\Delta}_{DES}^{II}$ differs from the original expression solely based on the local grid characteristic size $\Delta_{DES} = \Delta_{max} = max(\Delta_x, \Delta_y, \Delta_z)$ from Spalart et al. (1997). Instead, $\tilde{\Delta}_{DES}^{II}$ also uses the sub-grid length scale Δ_ω based on the local vorticity (ω) orientation and the local grid size (Chauvet et al., 2007):

$$\Delta_\omega = \sqrt{N_x^2\Delta_y\Delta_z + N_y^2\Delta_z\Delta_x + N_z^2\Delta_x\Delta_y} \quad (8)$$

Where $N_i = \frac{\omega_i}{||\omega||}$ is the unit vector which defines the orientation of the vorticity. The sub-grid length scale Δ_ω possesses the advantage to be flow dependent if the vorticity is not zero and determines the minimum length scale that the grid can resolve based on the flowfield. The use of Δ_ω has been proven to improve the development of the instabilities by reducing the level of eddy viscosity (ν_t) within separated regions and mixing layers (Deck, 2011). However, the use of the sub-grid length scale Δ_ω is not recommended for Eq. 6 as it strongly reduces the level of eddy viscosity, which can increase the tendency to Model Stress Depletion close to the wall. Therefore, for mode 2, the sub-grid length scale is implemented as follows:

$$\tilde{\Delta}_{DES}^{II} = \begin{cases} \Delta_{max} & if \quad f_d < f_{d0} \\ \Delta_\omega & if \quad f_d > f_{d0} \end{cases} \quad (9)$$

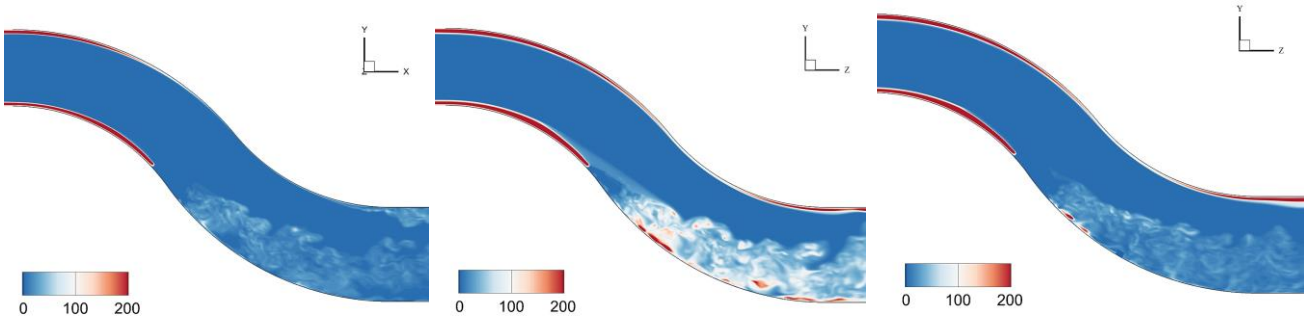

a) ZDES with $f_{d0} = 0.8$ **b) ZDES with $f_{d0} = 1$ (equivalent to DDES)** **c) ZDES with $f_{d0} = 1$ for the upper boundary layer and 0.8 elswehere**

Figure 5 Instantaneous distribution of ν_t/ν at the symmetry plane for different f_{d0} configuration for the baseline

Where $f_{d0} = 0.8$. Therefore, the ZDES mode 2 uses the blending function to determine which sub-grid length scale to apply. The use of Δ_{max} is guaranteed within the inner part of the boundary layer which is mandatory to properly shield the boundary layer. The outer bound of the boundary layer ($f_{d0} = 0.8$) used the sub-grid length scale Δ_{ω}.

3.4. Sub-grid length scale sensitivity

The use of Δ_{ω} is parametrised as in Eq. 9 with a f_{d0} value of 0.8. If the value of f_{d0} is set to 1 for the entire domain, the sub-grid length scale Δ_{max} is systematically used, which is equivalent to a DDES as defined by Spalart et al. (2006). The switch from RANS to LES is enhanced when the hybrid length scale $\tilde{\Delta}^{II}_{DES}(\Delta_{\omega})$ is used which demonstrates very low level of ν_t/ν from 25 to 50 within the separated flow region (Figure 6a). In comparison, the DDES with $f_{d0} = 1$ generates larger values of ν_t/ν from 40 to 140 within the separated flow field with a peak value of 200 (Figure 6b). The presence of higher levels of ν_t/ν induced by the advection of the upstream RANS eddy viscosity can lead to a reduction of the turbulent length scale resolved by the LES model. Therefore, the ZDES provides a better solution of the separated region within the S-duct compared with the DDES.

However, the use of Δ_{ω} can lead to grid induced separation for attached boundary layers under adverse pressure gradient, especially for refined grids. In this case, the blending function f_d fails to protect the attached boundary layer in the upper region of the S-duct. The switch from RANS to LES occurs within the boundary layer and leads to a grid induced separation at the exit of the S-duct (Figure 5a). The grid-induced separation significantly modifies the flow field with the generation of non-physical secondary losses and can alter the whole unsteadiness of the flow field at the AIP. The solution provided by the DDES demonstrated results that are more satisfactory with higher levels of eddy viscosity ratio associated with the upper boundary layer (Figure 5b).

One of the main advantages of the ZDES is the flexibility provided by the code regarding the type of flow model used for a specific application. The user can prescribe multiple turbulent models and numerical schemes over specific regions of the grid in order to satisfy the requirement of the simulation. A zonal allocation of the hybrid length scale $\tilde{\Delta}^{II}_{DES}$ was performed by setting the blending function threshold f_{d0} equal to 1 in the upper part of the S-duct. This ensures the use of the more conservative sub-grid length scale Δ_{max} based on the maximum cell size, which is less subject to model stress depletion due to local grid refinement. As a result, the solution demonstrates an attached boundary layer in the upper region of the S-duct and low levels of ν_t/ν within the main separated region (Figure 5c). Therefore, due to the nature of the flow and the refined grid used, the choice of the sub-grid length scale was not as straightforward as expected. The knowledge

from previous experimental studies (Gil-Prieto et al., 2017a; Tanguy et al., 2017) has proven to be useful to set up the computations.

3.5. Numerical scheme

The ZDES mode 2 (Deck, 2011) is used to address the location of the main separation region within the S-duct which was not known a priori. Based on the sensitivity analysis, the final allocation of the hybrid length scale $\widetilde{\Delta}_{DES}^{II}$ is reported in Figure 6. The 2nd order AUSM + (P) MiLES spatial discretization scheme (Mary and Sagaut, 2002) with a 3rd order limiter (Edwards and Liou, 1998; Mary et al., 2000) is used for the computation of the convective fluxes. The AUSM+ (P) is adapted for simulation with local regions of low Mach number due to the formulation of the dissipation terms, which is proportional to the local fluid velocity. The discretization scheme was also used as the reference scheme for the development of the ZDES (Deck, 2011) and was successfully used within previous ZDES studies (Deck et al., 2014, 2011; Mary and Sagaut, 2002; Richez et al., 2015). The diffusing fluxes are calculated by means of a 2nd order centred scheme. The time integration scheme used for the unsteady simulation is the Gear scheme which is a 2nd order accurate dual time step implicit scheme (Gear, 1971). This allows the resolution of the unsteady flowfield using sub-iterations of calculations between two physical instants. The choice of the physical time step for the simulation is guided by the Courant-Friedrichs-Lewy (CFL) number. A physical time step of $2.5 \times 10^{-7} s$ is chosen to maintain a CFL value less than 30 close to the wall (within the first 2 cells) and CFL values less than 1 for the main flowfield. For each physical time step, 4 sub-iterations are used to lower the residuals by an order of magnitude. Each ZDES calculation is initialised by a converged RANS solution as a starting point. For the baseline configuration, the ZDES was conducted over 120 convective times defined in Eq. 10, where L_s is the distance along the centreline of the duct and w_{ref} is the centreline reference velocity along the longitudinal direction at the reference plane (Figure 2).

$$\tau_c = \frac{L_s}{w_{ref}} \tag{10}$$

An initial transient period of $20\tau_c$ was discarded for the post processing to allow for the flow development between the initial RANS solution and the established LES solution. The choice of τ_c is based on previous DDES calculations (Gil-Prieto et al., 2017b) and the assessment of the AIP mass flow and total pressure ratio (PR). The duration of the transient phase strongly depends on the configuration investigated. For the vortex generators configurations, the time duration of the transient phase is reduced to a value of $10\tau_c$ based on the assessment of the standard deviation of the AIP mass flow and total pressure ratio. However, for consistency, a total of $20\tau_c$ was also removed from the start of all simulations.

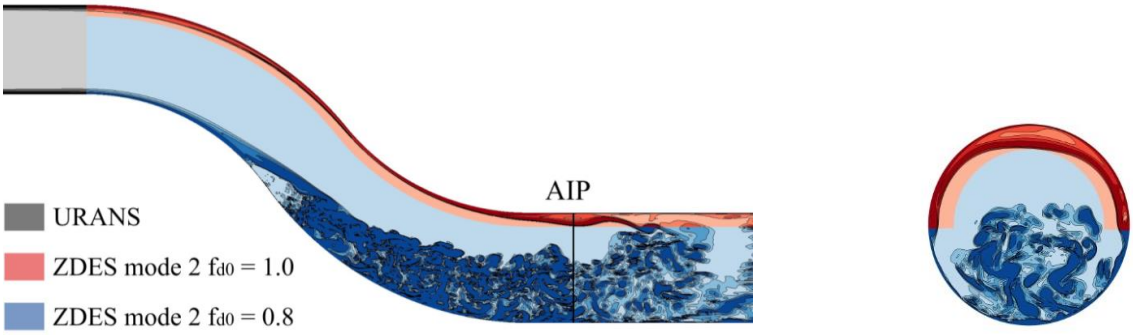

a) Symmetry plane **b) AIP**

Figure 6 Instantaneous distribution of the vorticity magnitude shaded with the zonal allocation of the ZDES parameters for the baseline configuration

4. Results and discussion

4.1. Flowfield overview

Instantaneous flowfield

For the baseline configuration, the flowfield separates after the first bend on the lower surface which induces a region of high unsteadiness characterised by the formation of eddies and turbulent structures which are convected to the exit of the S-duct (Figure 7a). As a result, the well-identified loss region (Garnier, 2015; Tanguy et al., 2018) is present at the AIP with a deficit in total pressure ($P_0/P_{0,ref}$) with values as low as 0.89 (Figure 7a, right). Downstream of the separation, the turbulence is resolved as the calculation switches from RANS to LES mode. The instantaneous solution at the symmetry plane indicates a delay in the formation of the flow instability and unsteadiness initiated by the separation. This flow feature is identified by the absence of turbulent structures downstream of the separation point and caused by the switch from RANS to LES model (Figure 7a, left). Once the model switches from RANS to LES, the main mechanism that promotes the development of the unsteadiness is the flow separation. However, due to the absence of inflow turbulence and the low velocity flow downstream of the separation point, the development of the unsteadiness is slow. A further refinement of the mesh would not improve the solution. The use of a Wall-modelled LES such as the ZDES mode 3 (Deck et al., 2011), which resolve the turbulent flow within part of the boundary layer even when attached, should improve this aspect with an instantaneous development of the flow instabilities at the separation point. However, the injection of appropriate turbulence in the upstream flow and within the boundary layer is needed for these methods, which requires calibration and further knowledge on the upstream conditions. The use of the ZDES mode 3 is not feasible from an industrial application yet and beyond the scope of this paper.

The instantaneous flowfield for the baseline highlights a shear layer where both small and larger scale turbulent structures are present and are susceptible to induce large vertical fluctuations of the loss region at the exit of the S-duct (Figure 7a, left). The boundary layer on the upper surface of the S-duct does not demonstrate any turbulent unsteadiness due to the use of URANS in this region. However, the fluctuations of the main loss region can impact the dynamic of the top boundary layer.

The iso-surface of the Q-criteria coloured by the non-dimensional streamwise velocity is used to highlight the main flow features (Figure 7a, right). The streamwise velocity (Vs) is calculated as the normal velocity component to the local cross section perpendicular to the S-duct centreline. The flow separation generates coherent vortical structures associated with a range of non-dimensionalised streamwise velocities ($Vs/\langle\overline{w}_{AIP}\rangle$). Annular shaped vortices are particularly visible within the mixing layer and convected at a high velocity close to $\langle\overline{w}_{AIP}\rangle$. Previous studies (Gil-Prieto et al., 2017b, 2017a) demonstrated that the flow unsteadiness was not only driven by the main separation region but also by the rise of secondary flows. The unsteady secondary flows are responsible for the swirl switching mode commonly investigated in bended pipe flow (Gil-Prieto et al., 2017a, 2017b; Kalpakli Vester et al., 2015; Tunstall and Harvey, 1968). This flowfield oscillation can be identified from the iso-surface of the Q-criteria which indicates a coherent oscillation from left to right of the separated flow (Figure 7a, right).

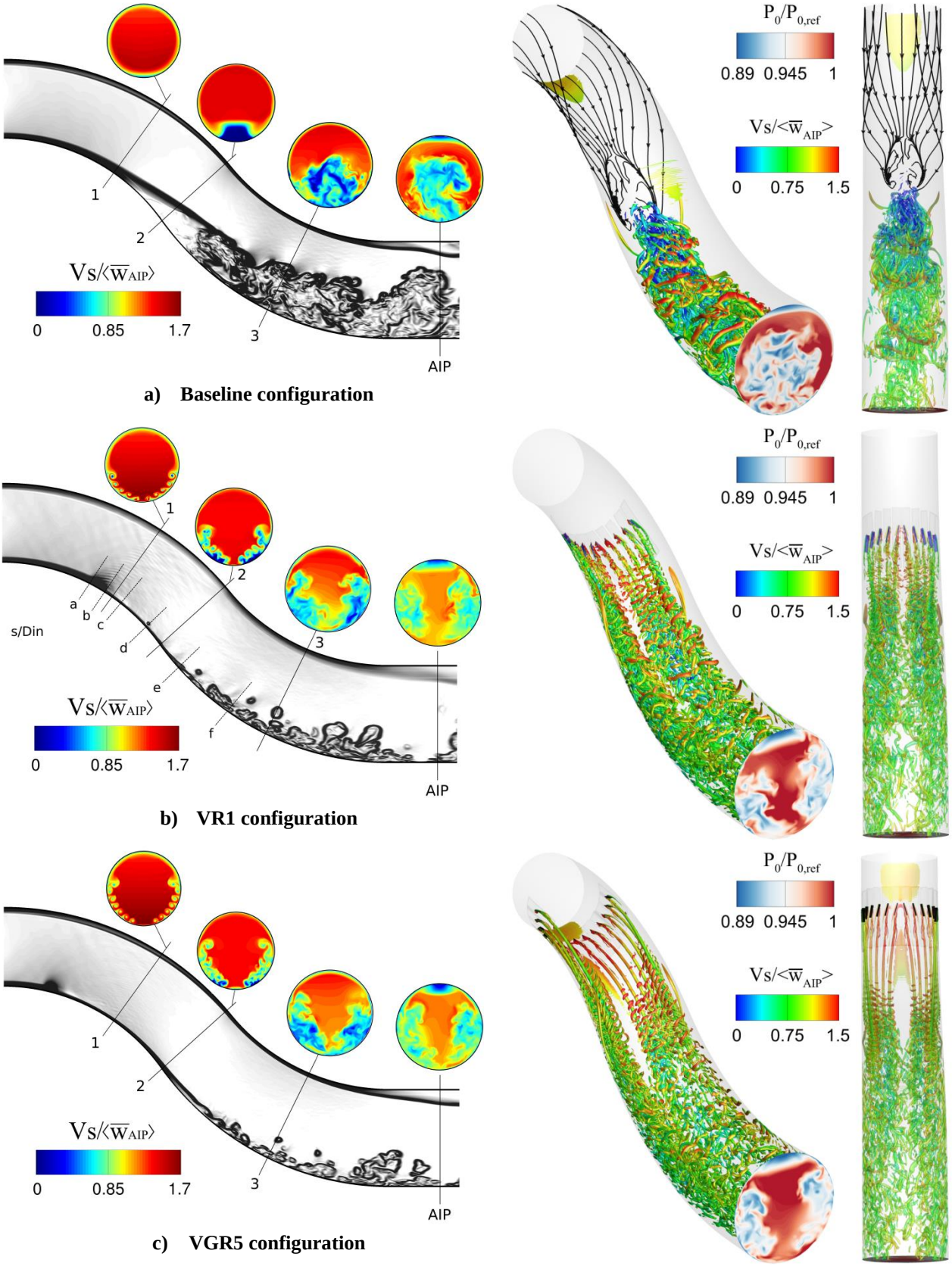

a) Baseline configuration

b) VR1 configuration

c) VGR5 configuration

Figure 7 Snapshot of ZDES instantaneous flowfield. Left column: Density gradient modulus at the symmetry plane and streamwise velocity ($Vs/\langle\bar{w}_{AIP}\rangle$) at several S-duct cross sections. Right column: Q-criteria coloured by the streamwise velocity and the distribution of the total pressure ($P_0/P_{0,ref}$) at the AIP

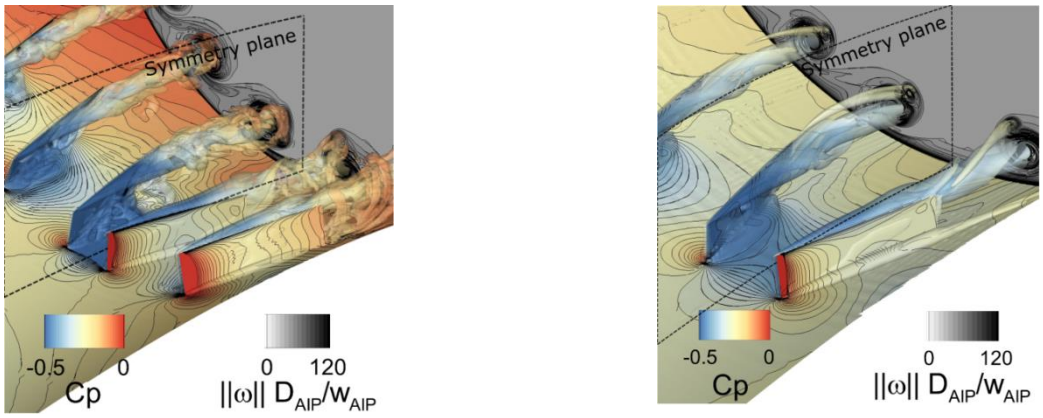

a) VGR1 **b) VGR5**

Figure 8 Visualisation of the vortex formation by Q-criteria in the VG regions. Flow direction is from left to right.

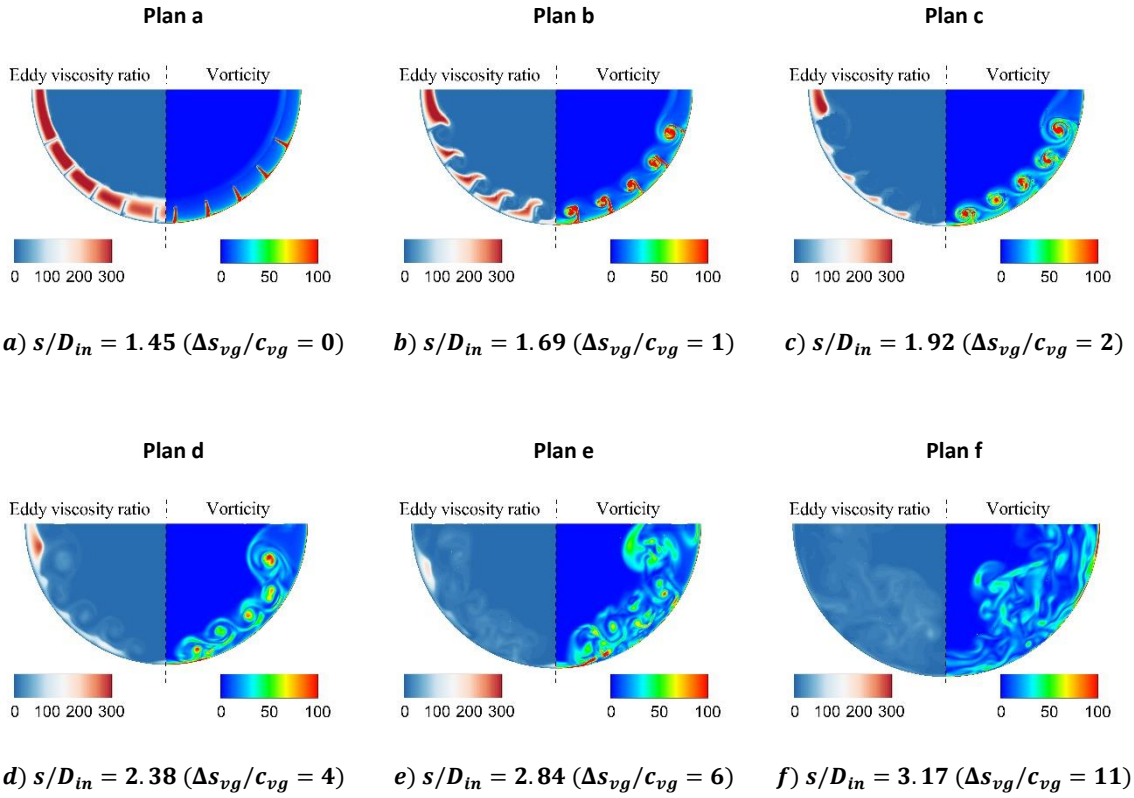

$a)\ s/D_{in} = 1.45\ (\Delta s_{vg}/c_{vg} = 0)$ $b)\ s/D_{in} = 1.69\ (\Delta s_{vg}/c_{vg} = 1)$ $c)\ s/D_{in} = 1.92\ (\Delta s_{vg}/c_{vg} = 2)$

$d)\ s/D_{in} = 2.38\ (\Delta s_{vg}/c_{vg} = 4)$ $e)\ s/D_{in} = 2.84\ (\Delta s_{vg}/c_{vg} = 6)$ $f)\ s/D_{in} = 3.17\ (\Delta s_{vg}/c_{vg} = 11)$

Figure 9 Instantaneous flowfield for ν_t/ν and $|\omega|D_{in}/\langle\overline{w}_{AIP}\rangle$ at different cross section along the centreline s/D_{in} for the configuration VGR1. See Figure 7b for plan location a-g.

The use of vortex generators has a strong impact on the flowfield within the S-duct. The vortex generators provide an attached flowfield with the suppression of the main recirculation region at the symmetry plane (Figure 7b and c). The use of vortex generators changes drastically the flowfield topology within the S-duct. The VGs generate a set of trailing vortices that prevent the rise of the initial secondary flows and suppress the separation region at the lower surface of the S-duct. However, the VGs are also responsible for the formation of small-scale coherent structure associated with the VG wake (Figure 7b and c). Toward the exit of the S-duct, the trailing vortex patterns breakdown to merge into a more uniform

turbulent region. As a result, the main loss region at the AIP identified for the baseline configuration is replaced by two distinct loss regions on each side of the vertical axis.

The trailing vortices generated by the VGs present different characteristics for VGR1 and VGR5 (Figure 8). For both configurations, there is a separation on the suction side of the VGs which is initiated at the leading edge. The main vortex is formed by the roll-up of the flow over the tip of the VG which generates a strong vorticity component in the longitudinal direction. A small corner vortex is also generated at the root of the VGs on the positive pressure side. For VGR1, the Q-criterion highlights the fluctuations of the flowfield associated with the vortices generated by the VGs with the presence of additional eddies around the main vortex core. For VGR5, the flow after the VG presents fewer fluctuations of the vortical structures compared with VGR1. A secondary vortex can also be observed from the trailing edge of the VGs which rolls up around the main vortex core for VGR5 (Figure 8b). The qualitative assessment of the time dependent flowfield shows that the ZDES calculation is able to capture some unsteadiness associated with the trailing vortices generated by the VGs. The uses of VGs have a strong impact on the flowfield topology within the S-duct. The large unsteady separated region for the baseline configuration is suppressed and replaced by a more symmetric flowfield with smaller scale structures convected to the AIP.

Eddy viscosity behaviour

To analyse the behaviour of the hybrid RANS/LES model when vortex generators are used, the eddy viscosity ratio is compared at several locations downstream of the vortex generators for the VGR1 case (Figure 9). The S-duct cross-sections have been chosen to be located at a distance of 0, 1, 3, 5, 10 and 15 chord lengths (c_{vg}) from the leading edge of the VG (Δs_{vg}). Ideally, the flowfield following the vortex generators needs to be modelled using a LES solution in order to fully capture the development of the unsteady flow. However, the small distance between the vortices and the wall can promote the grid ambiguity by placing the "grey area" close to the wall. The use of the chimera grid enables local refinement of the mesh around the VGs to achieve a grid resolution appropriate for LES calculations. However, the absence of turbulent content from the incoming boundary layer could also impact the development of the vortices issued from the VGs.

The flowfield at the leading edge of the vortex generators is modelled with URANS as it presents high values of eddy viscosity ratio with $\nu_t/\nu > 300$ (Figure 9a). A rapid destruction of ν_t/ν is present on the suction side of the vortex generators caused by a local flow separation (Figure 8a). At a distance from the leading edge of the VGs (Δs_{vg}) of 2 chords (c_{vg}), each VG has generated a vortex of similar size and intensity. The vortices result in low levels of $\nu_t/\nu > 25$ meaning that the LES model is used to resolve the turbulent content of the vortices. However, the level of ν_t/ν still demonstrates the use of URANS close to the wall and within vortices cores (Figure 9c). At a distance of 4 chords from the leading edge of the VGs, the outermost vortex is detached from the S-duct surface (Figure 9d) and rolls up around its neighbour. The level of ν_t/ν at a position of $6c_{vg}$ from the leading edge of the VGs (Figure 9e) is reduced even close to the wall to finally be equal to 20 in the unsteady flow region (Figure 9f). Therefore, the structure of the trailing vortices generated by the VGs is completely changed into a more homogenous turbulence flow at $\Delta s_{vg}/c_{vg}$=11 and is resolved using the LES model.

Time averaged flowfield

The time-averaged and standard deviation distributions of the full flowfield were calculated based on the simulated period after the initial transient was discarded. The time averaged static pressure coefficient (C_p) distribution along the S-duct wall is compared with the experimental data for three circumferential angles $\phi = 10°, 90°$ and $170°$. For the baseline configuration (Figure 10a), the main separation region can be identified by the static pressure plateau along the position $\phi =$

170°. The experimental separation and reattachment point location at the symmetry plane were identified from flow oil visualisation. For the CFD results, the time averaged position of the separation and reattachment points were identified from the position where the wall shear stress is close to zero combined with the presence of a saddle point based on time averaged wall skin-friction lines. The location of the separation and reattachment points for the baseline configuration are annotated in Figure 10a. For the experimental data, the separation point along the curvilinear distance was measured at a distance of $s/D_{in} = 1.97$ and the reattachment point was near the position $s/D_{in} = 3.70$. The time-averaged ZDES demonstrates a separation point located at $s/D_{in} = 2.12$. As a result, the Cp values associated with the pressure plateau for the CFD solution are higher than for the experimental data with $Cp = 0.15$ and 0.05 for the CFD and experimental solution respectively (Figure 10a). For the experimental results, the length of the wall static pressure plateau is about 50% of the separation length, L_{sep} (distance projected along the curvilinear distance s). This was also previously observed experimentally (Garnier, 2015) based on steady and unsteady wall static pressure measurement for the same S-duct geometry. However, the length of the Cp plateau is over estimated by the ZDES data which is about $0.75L_{sep}$. As a result, the recompression downstream the static pressure plateau is stronger for the ZDES than for the experiments. However, the centreline location of the reattachment point for the CFD results is in agreement with the experimental one identified from the oil flow visualisation (Figure 10a).

The use of vortex generators suppresses the region of constant static pressure which indicates that the flow remains attached along the centreline of the S-duct (Figure 10b and c). For VGR1, the impact of the vortex generators on the static pressure is visible with the sudden local Cp reduction around $s = 1.5D_{in}$ for the ZDES. This is not captured by the experimental data due to the significantly lower spatial resolution of the measurements. Nevertheless the recompression after the vortex generators is well captured by the ZDES which demonstrates that the flowfield behind the vortex generators is properly modelled. However, the level of Cp for the position $\phi = 90°$ (side wall) is over predicted near the S-duct exit which could indicate an under prediction of the velocity within this region at the AIP. Relative to the baseline configuration, the range of Cp value on the upper wall along the position $\phi = 10°$ is reduced when the vortex generators are used (Figure 10b and c). The blockage induced by the centreline separation for the baseline is decreased when the VGs are used. As a result, the flow on the upper section of the duct is less accelerated due to the second bend. Therefore, the comparison of the wall static pressure coefficient computed from the ZDES is in agreement with the measured data.

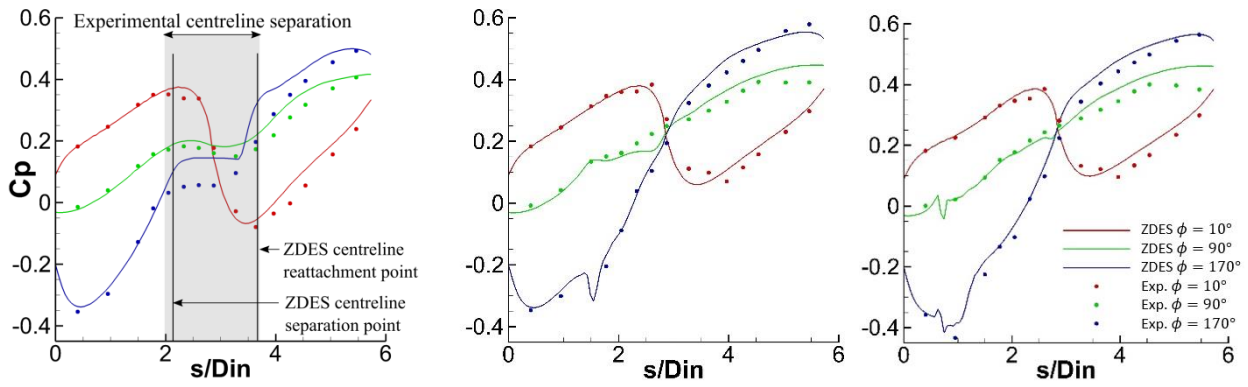

a) Baseline b) VGR1 c) VGR5

Figure 10 Comparison between the ZDES and experimental time-averaged wall static pressure coefficient within the S-duct

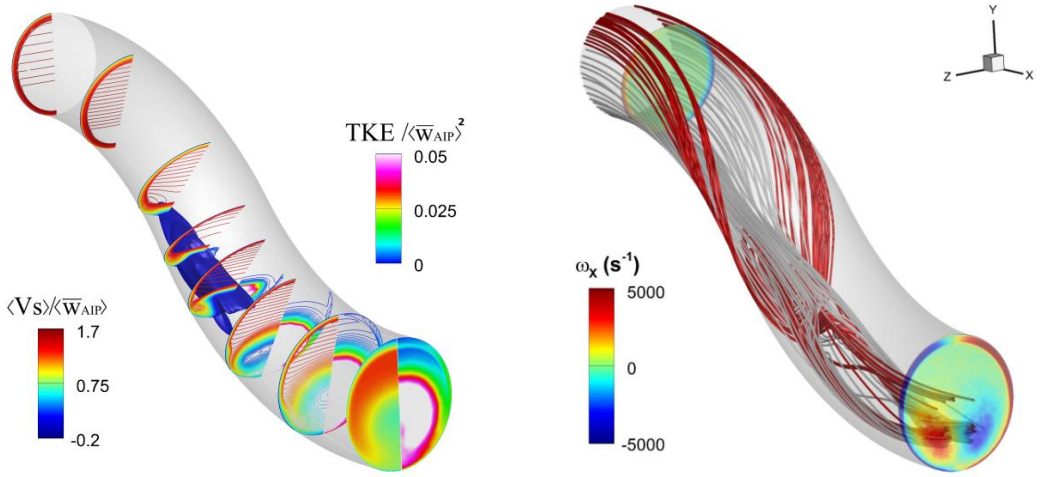

a) Baseline configuration

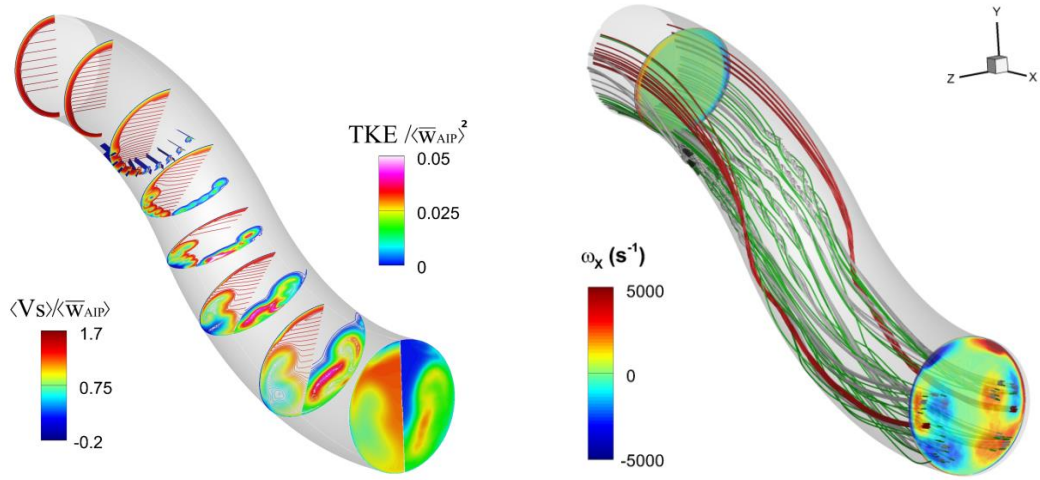

b) VGR1 configuration

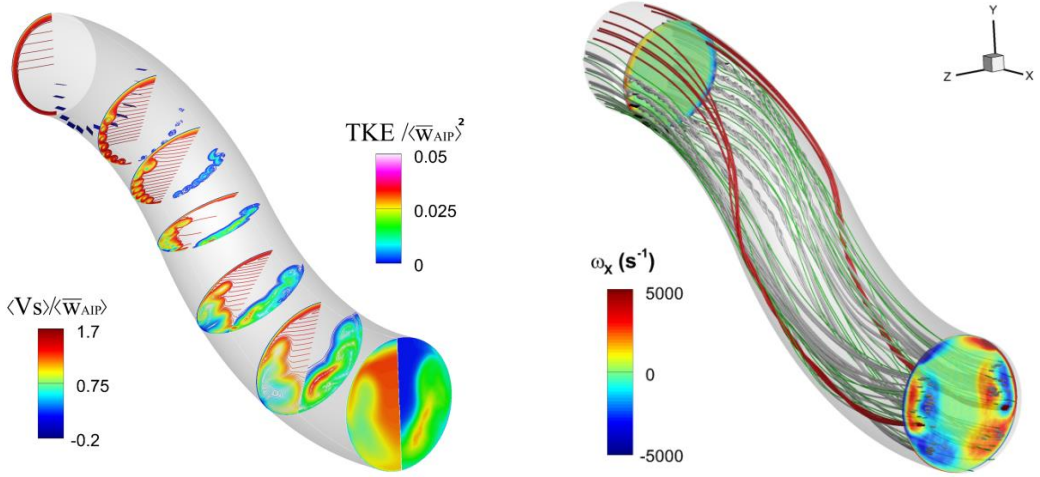

c) VGR5 configuration

Figure 11 ZDES time-averaged flowfield. Left column: Cross sections of the non-dimensionalised streamwise velocity (port) and resolved turbulent kinetic energy (starboard). Right column: Velocity streamlines and out-of-plane vorticity.

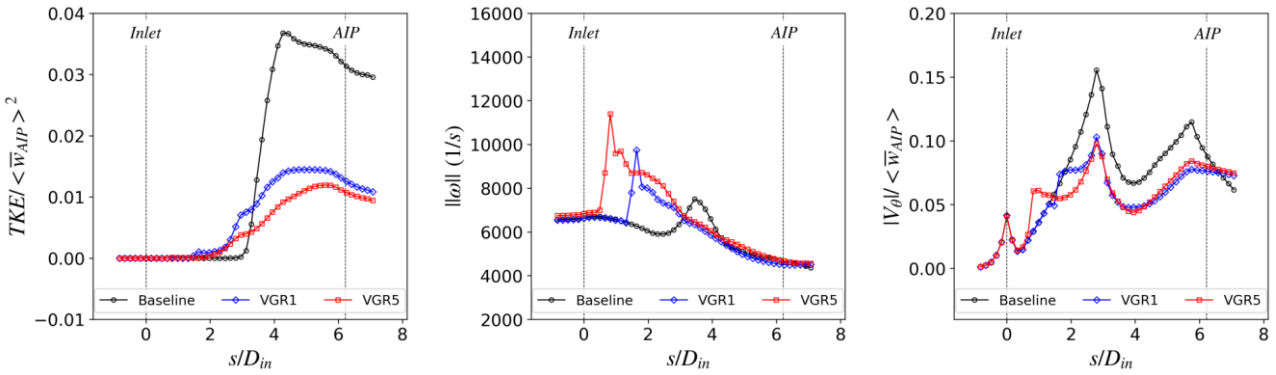

a) Non-dimensionalised resolved TKE **b) Vorticity magnitude** **c) Absolute circumferential velocity**

Figure 12 Streamwise distribution of the cross-sectional area-weighted average flowfield along the S-duct

The time averaged flow and 3D velocity streamlines are computed in order to provide an overview of the flow topology within the S-duct (Figure 11). For the baseline configuration, the separation region is identified from the iso-surface of null streamwise velocity (Figure 11a). The streamwise distribution of the cross-sectional area-weighted average flowfield along the S-duct is reported in Figure 12. The deficit in streamwise velocity is convected to the AIP and is associated with a rise of the resolved turbulent kinetic energy (turbulent kinetic energy based on the time resolved velocity fluctuations) (Figure 12a). The secondary flows induced a peak of area-weighted average vorticity near the reattachment point (Figure 12b) which initiates the twin vortex cores present at the AIP (Figure 11a).

As for the instantaneous flowfield, the vortex generators affect the flow topology by suppressing the initial secondary flows (Figure 11b and c). The trailing vortices generated by the VGs force the flow within the lower half of the duct to remain along the streamwise direction. However, some initial features induced by the duct curvature are still present and highlighted by the red streamlines in Figure 11. The vorticity field at the AIP for the VG configurations (Figure 11b and c) exhibits a pair of vortices rotating in the opposite sense to that of the baseline configuration. The area-weighted average vorticity at the S-duct exit is very similar for the three configurations despite the peak induced by the vortex generators within the S-duct (Figure 12b). The level of area-weighted average absolute swirl velocity ($|V_\theta|/\langle \overline{w}_{AIP} \rangle$) at the AIP is also similar for the baseline and the VG configurations (Figure 12c). However, within the S-duct, the level of V_θ is reduced for the VG cases and nearly constant between the S-duct exit and the AIP.

In addition, the VG configurations have a strong impact on the level of unsteadiness. The non-dimensionalised resolved turbulent kinetic energy is reduced by more than half within the S-duct when VGs are used (Figure 12a). For the VG configurations, the main unsteadiness is issued from the VG wakes and stays confined within the loss regions (Figure 11). Based on the TKE distribution, the unsteadiness associated with VGR1 is higher than for VGR5 (Figure 12a). However, very similar levels are achieved at the AIP for both VG configurations.

4.2. Assessment of the AIP flowfield

AIP flowfield statistics

The time averaged flowfield from the experimental data is compared with the time averaged ZDES solutions (Figure 13). The AIP spatial discretisation for the CFD results has been reduced to match the total pressure and S-PIV measurement resolutions. Due to laser light reflection and seeding oil contamination, the S-PIV AIP flowfield near the wall $r/R > 0.95$ has been removed and is not taken into account for the analysis of the flow statistics. This also coincides with the location of the nearest to the wall steady total pressure probe at the AIP. Similarly, the flowfield extracted from simulations for

$r/R > 0.95$ is also discarded for the computation of the area weighted statistics of numerical data. Therefore, the experimental and numerical AIP flow fields are compared using the same spatial resolution and integrals value are calculated over the same AIP area.

For the baseline configuration, the time averaged total pressure ratio (PR) defined as $\langle\overline{P_0}\rangle/P_{0,ref}$, is predicted with less than 0.2% difference relative to the experimental data which is within the uncertainty of the measurements (Table 1). The measured and simulated total pressure (Figure 13a, f) and out-of-plane velocity (Figure 13b, g) show a good agreement in term of flow topology and loss value. However, it can be noticed that the total pressure level within the high momentum region for the experimental data is slightly lower than for the numerical results (Figure 13a, f). The Pitot probes used for the steady total pressure measurements are expected to be insensitive to flow angularity up to about $\pm 10°$. As a results, the high angularity of the instantaneous velocity flow field at the AIP could contribute to an under estimation of the experimental time averaged total pressure compared with the CFD. It can also be noticed that the ZDES solution slightly over predicts the size of the main loss region associated with lower levels of total pressure compared with the experimental data. The steady pressure measurements are performed with low bandwidth pressure transducers pneumatically connected to the Pitot probes. As a result, it is expected that high frequency low pressure fluctuations to be partially damped, which can contribute to the underestimation of the total pressure within region of high unsteadiness. Overall, the in-plane components of the velocity field indicate a small over prediction of the secondary flows by the ZDES for the lower half of the section (Figure 13h, i).

The ZDES solution also provides a fair agreement with the experimental upper boundary layer in terms of losses, extent and intensity. The swirl angle distribution indicates higher levels of $|\alpha|$ at the centre of the section compared with the experimental data (Figure 13j, d). As a result, the absolute time-averaged swirl angle value is over predicted by 0.8° for the ZDES solution compared with the S-PIV data. Overall, the use of high spatial resolution total pressure and S-PIV measurements demonstrates that the ZDES for the baseline is in good agreement with the experiment in terms of flow topology and total pressure losses. In addition, the level of area-weighted average total pressure and swirl angle predicted by the ZDES is in agreement with the experimental data (Table 1).

Table 1 Comparison of the area iweighted statistics at the AIP

	Baseline		VGR1		VGR5	
	Exp.	ZDES	Exp.	ZDES	Exp.	ZDES
M_{ref}			0.60			
PR	0.958	0.960	0.964	0.964	0.966	0.965
$\bar{\sigma}_{P_0}/q_{AIP}$	0.34	0.34	0.21	0.19	0.17	0.20
$\langle\overline{w}_{AIP}\rangle/w_{ref}$	0.621	0.626	0.632	0.621	0.628	0.616
$\bar{\sigma}_w/\langle\overline{w}_{AIP}\rangle$	0.17	0.15	0.09	0.09	0.08	0.08
$\langle\overline{\lvert\alpha\rvert}\rangle$ (°)	3.9	4.7	3.9	4.1	3.9	4.4
$\bar{\sigma}_\alpha$ (°)	9.8	8.8	5.0	5.3	4.6	4.7
$TKE/\langle\overline{w}_{AIP}\rangle^2 \times 10^2$	4.14	3.46	1.21	1.34	1.05	1.09

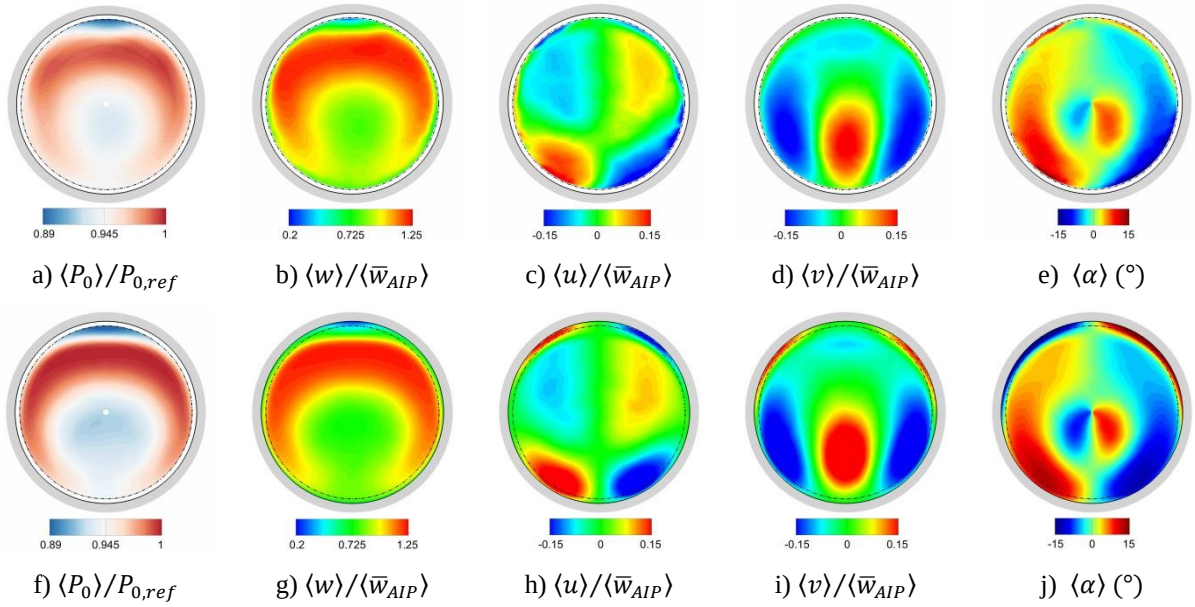

Figure 13 Flow time averaged comparison with the experiment (top) and the ZDES (bottom). The experimental total pressure (a) is based on steady measurements, the velocity and swirl distribution are based on S-PIV data (b-e)

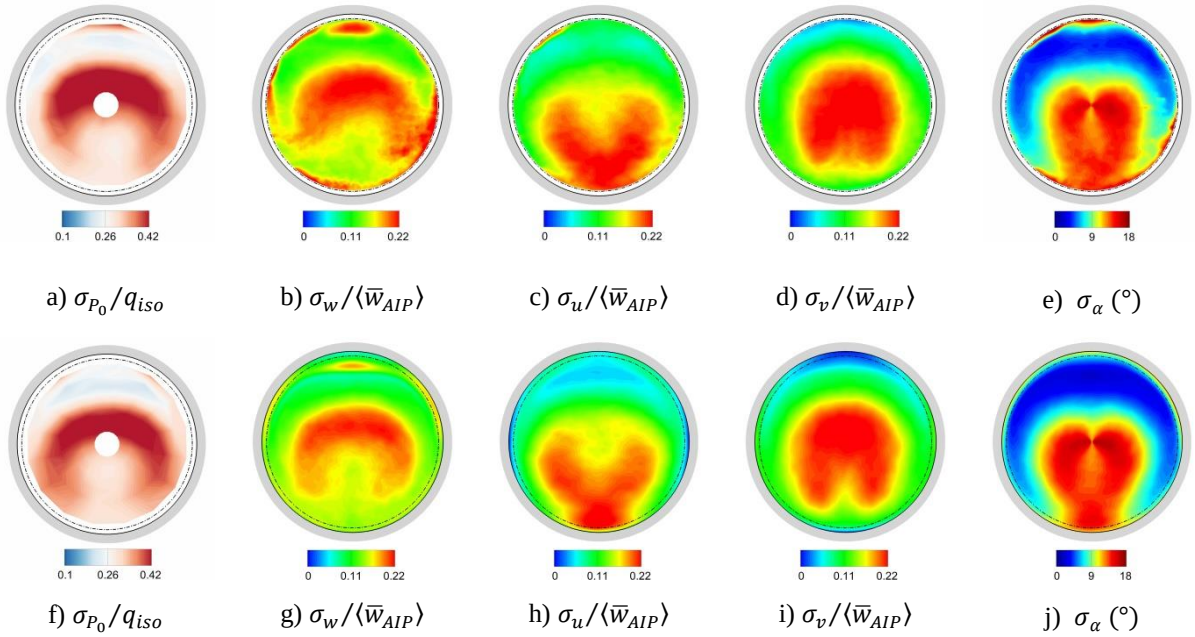

Figure 14 Flow standard deviation comparison with the experiment (top) and the ZDES (bottom). The unsteady total pressure (a) was measured with high frequency response Pitot probes, the velocity and swirl distribution are based on S-PIV data (b-e)

The unsteady flowfield from the ZDES solution is directly compared with the experimental total pressure and S-PIV data. The velocity and swirl angle fluctuations are in broad agreement with the S-PIV data demonstrating that the main flow unsteadiness is correctly reproduced by the ZDES calculations (Figure 14b-e, g-j). The level of out-of-plane velocity fluctuations is slightly lower than the experimental one with predicted area weighted value of $\bar{\sigma}_w/\langle \bar{w}_{AIP} \rangle$ of 0.15 compared with 0.17 for the S-PIV data (Table 1). Both simulated and measured flowfield show a predominant rise of the unsteadiness in the central part of the AIP, surrounding the region of time averaged loss region. The ZDES calculation also demonstrates high level of unsteadiness with peak of $\sigma_w/\langle \bar{w}_{AIP} \rangle$ of 0.21 located in the flowfield near the upper periphery of the AIP (Figure 14g). This region of high unsteadiness has a reduced extent for the ZDES compared with the S-PIV experiment (Figure 14b). This region is of particular interest as it represents an attached boundary layer subject to high unsteadiness and is a challenging feature to simulate with a hybrid RANS/LES model. The peak in unsteadiness near the top of the AIP is also visible with the measured total pressure field (Figure 14a). However, the overall level of fluctuations of total pressure is in agreement with the experimental data (Figure 14f).

The use of vortex generators changes the level of total pressure and out-of-plane velocity losses and induces new secondary flows at the AIP. The main central loss region for the baseline configuration is replaced by two symmetrical regions of low total pressure and out-of-plane velocity from each side of the centreline axis (Figure 15a, b). For both experimental and numerical data, the development of a pitching down component of the flowfield along the centreline axis of the AIP is observed (Figure 15c, j). The swirl angle distribution demonstrates for both results, a dominant contra-rotating pair of vortices (Figure 15c, j) located in the lower half of the AIP. For VGR1, a similar level of absolute swirl angle $\langle \overline{|\alpha|} \rangle$ for the ZDES and S-PIV results of 3.9° and 4.1° respectively is shown (Table 1). The total pressure ratio predicted by the ZDES is in agreement with the measured data which indicates about 0.6% improvement of PR compared with the baseline configuration which may be of interest depending of the context of the application (Table 1). However, the time averaged out-of-plane velocity ratio $\langle \bar{w}_{AIP} \rangle / w_{ref}$ is slightly under predicted by the ZDES. The diffuser performance based on the velocity is predicted within 1% of the experimental data, which is of the order of the experimental uncertainty.

Although the intensity of the losses in total pressure and out-of-plane velocity ($\langle w \rangle / \langle \bar{w}_{AIP} \rangle$) at the AIP are well reproduced with the ZDES calculation, some differences in terms of flow pattern can be noticed between the numerical and experimental results. The extent of the two loss regions is larger for the CFD solution (Figure 15h). Additional clockwise and counter-clock wise swirling regions for respectively the left and right side of the AIP are formed near the side wall of the AIP (Figure 15i). The secondary loss region located near the upper periphery of the AIP caused by the second bend of the duct is slightly over predicted by the ZDES solution. The circumferential extent of the loss in total pressure (Figure 15g) and out-of-plane velocity (Figure 15h) near the upper wall is two times larger for the CFD results. However, the levels of out-of-plane velocity and swirl angle are in agreement with the experimental data close to the upper periphery of the section.

The use of vortex generators considerably affects the unsteadiness of the flowfield at the AIP compared with the baseline configuration. For VGR1, the distribution of the standard deviation of the flow variables is computed to assess the level of fluctuation associated with the flowfield (Figure 16). The regions of maximum total pressure fluctuations are located around the edges of the low total pressure regions with values of σ_{P_0}/q_{AIP} between 0.27 and 0.30 (Figure 16a, g). For the experimental results, the use of VGR1 reduces the area-averaged total pressure fluctuations by 38% compared with the baseline. The ZDES computation also similarly predicts the reduction in flow unsteadiness with a reduction of 44% of $\bar{\sigma}_{P_0}/q_{AIP}$ compared with the baseline (Table 1). The fluctuating levels of out-of-plane velocity and swirl angle (Figure 16h, i) for the ZDES are also in good agreement with the experimental data (Figure 16b, c). The value of $\bar{\sigma}_\alpha$ for the experimental

and CFD results are 5.0° and 5.3° respectively which corresponds to a reduction of swirl unsteadiness of 49% and 40% compared with the baseline configuration (Table 1). As for the time averaged solution, some minor differences in terms of the distribution of the fluctuations between the experimental and the ZDES solution can be identified. For the ZDES, the lower section of the AIP along the centreline axis is associated with moderate levels of flow fluctuation values of σ_{P_0}/q_{AIP} , and $\sigma_w/\langle\overline{w}_{AIP}\rangle$ respectively 0.25 and 0.1 (Figure 16g, f). These fluctuation levels cannot be identified for the experiment. The experimental results also demonstrate moderate level of fluctuations for the out-of-plane velocity and swirl associated with the loss in $\langle w\rangle/\langle\overline{w}_{AIP}\rangle$ near the upper periphery of the section, which mainly characterise a lateral oscillation of the upper boundary layer (Figure 16b and c). For the ZDES, the upper boundary layer oscillation is not captured (Figure 16h and i). This may be a consequence of the use of URANS model within the upper boundary layer which tends to stabilise the flowfield. The fluctuation levels associated with the two main loss regions on each side of the centreline axis for the ZDES are in agreement with the S-PIV results. However, peak values of σ_α up to 9.0° are present in the upper sector of the main symmetrical loss regions for the CFD while the experimental data presents value of σ_α around 5.5° at this location (Figure 16c, i). Overall, the unsteady flowfield based on fluctuation levels is well reproduced by the ZDES. The level of resolved turbulent kinetic energy ($TKE/\langle\overline{w}_{AIP}\rangle^2$) for the ZDES is slightly over predicted with an area-average value of 1.34×10^{-2} compared with 1.21×10^{-2} for the experimental results (Table 1). This could also be associated with the small under estimation of the averaged out-of-plane velocity at the AIP ($\langle\overline{w}_{AIP}\rangle/w_{ref}$).

The design parameters of VGR1 and VGR5 are significantly different. The configuration VGR5 is placed at a curvilinear distance $s/D_{in} = 0.74$ from the inlet of the S-duct while VGR1 is placed close to the baseline separation point at s/Din = 1.55. The height of VGR5 is significantly lower with $h_{vg}/\delta_{ref} = 0.91$, as opposed to $h_{vg}/\delta_{ref} = 1.27$ for VGR1. Furthermore, the configuration VGR1 and VGR5 are respectively made of 10 and 14 vortex generators. The effect of VGR5 on the flow structure is well captured by the ZDES with the presence of the two loss regions issued from the vortex generators close the wall (Figure 15e, k). The level of losses in total pressure associated with the CFD flowfield are also in agreement with the experimental data (Figure 15d, j). As a result, the computed PR for VGR5 is close to the measured data with PR = 0.965 and 0.966 for the ZDES and experimental data respectively (Table 1). For ZDES, the averaged level of absolute swirl angle $\langle\overline{|\alpha|}\rangle$ is over predicted by 0.5° compared with the S-PIV flowfield. This was also the case for the baseline configuration that predicted a value of $\langle\overline{|\alpha|}\rangle$ of 4.7° compared with 3.9° for the experimental results. A secondary swirling region associated with the upper part of the main loss regions for VGR5 can be identified which characterised two secondary vortices close to the wall on each side of the AIP (Figure 15l). This flow feature was also observed for VGR1 associated with modest swirl angle value. These secondary vortices are associated with higher values of swirl angle fluctuations (σ_α) around 8° for the ZDES while σ_α is about 5° for the experimental data (Figure 16f, l). However, the overall level of fluctuations at the AIP is well predicted with a difference of 0.1° for the area averaged value of swirl fluctuations ($\bar{\sigma}_\alpha$) and 0.04×10^{-2} for the resolved turbulence kinetic energy ($TKE/\langle\overline{w}_{AIP}\rangle^2$).

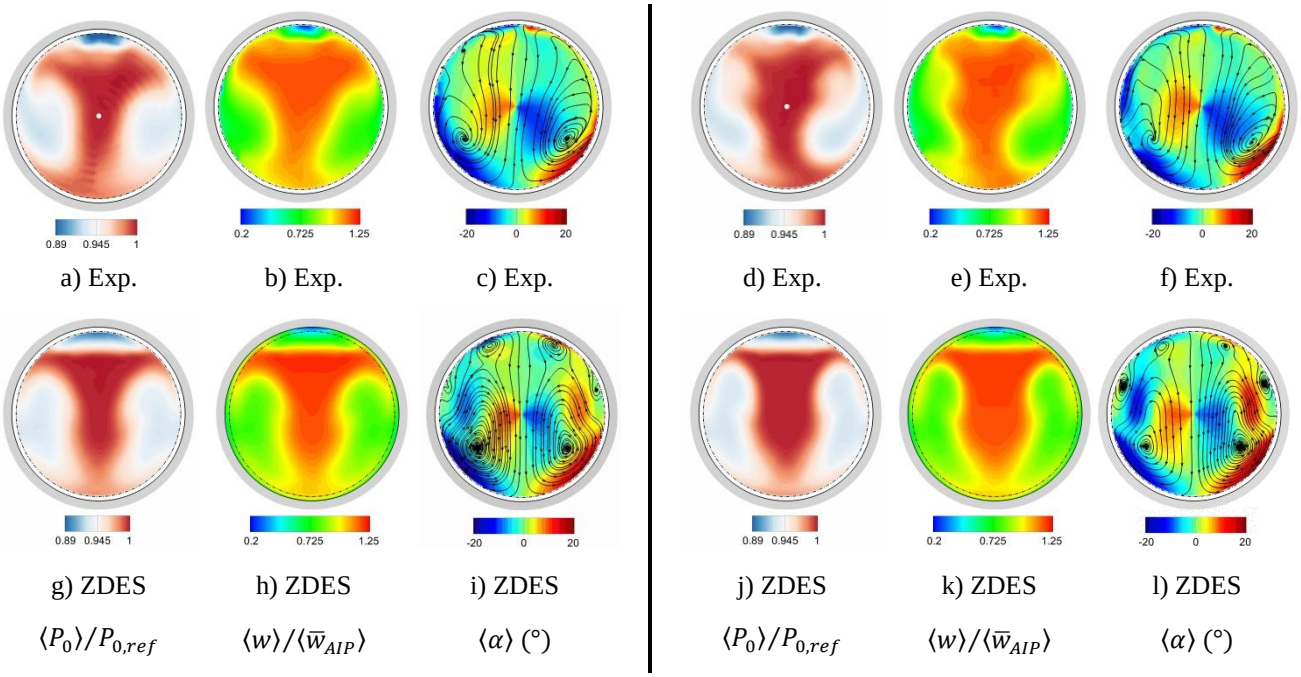

Figure 15 Comparison between the experimental (top) and ZDES time averaged flowfield with the flow control devices. The measurements are performed with steady total pressure rakes (a, d) and the S-PIV system

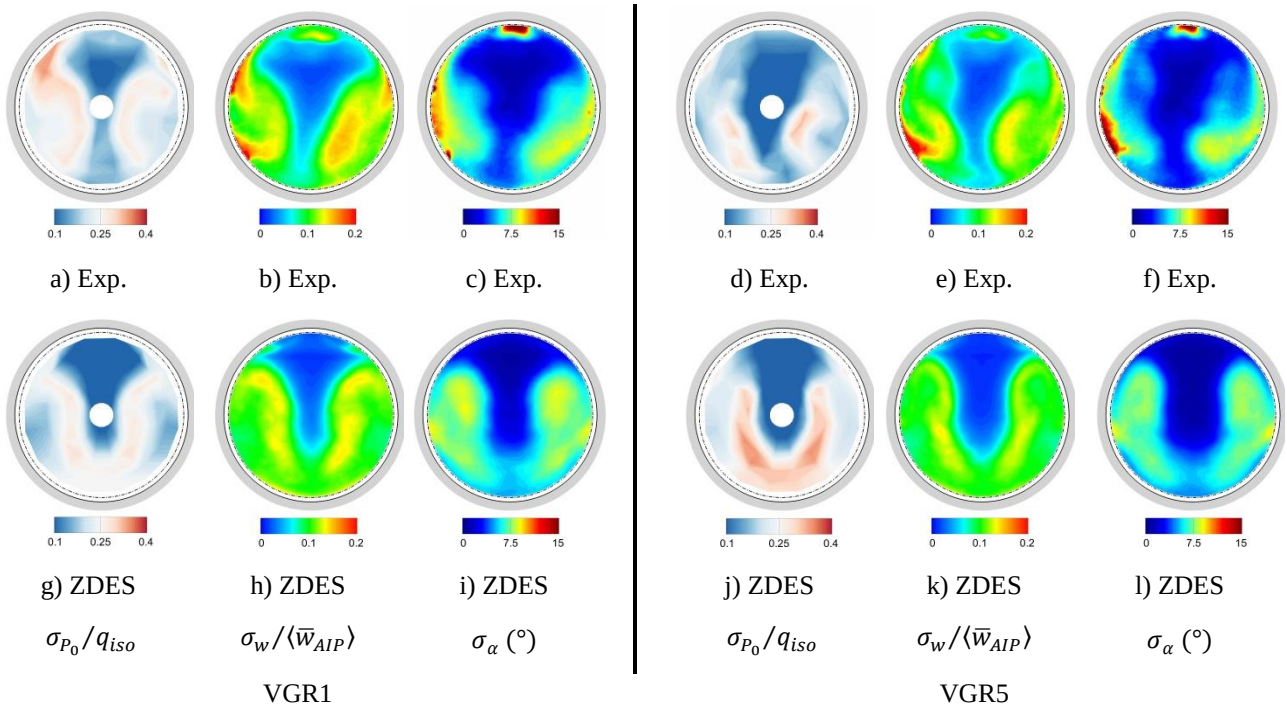

Figure 16 Comparison between the experimental (top) and ZDES fluctuating flowfield with the flow control devices. The measurements are performed with unsteady total pressure rakes (a,d) and the S-PIV system

Unsteady flow distortion at the AIP

The Society of Automotive Engineers (2007) swirl distortion descriptors are computed for the experimental and CFD data to characterise the swirl non-uniformities at the AIP. The AIP section is discretised into 9 rings, and each descriptor is calculated at each radial position based on the swirl angle (α) distribution. The swirl intensity descriptor SI calculates the averaged absolute swirl angle in the ring. The swirl directivity SD represents the overall sense of rotation of the swirling flow. The SD descriptors range from -1 and 1 to characterise respectively a clockwise and anticlockwise swirling structure. The swirl pair descriptor SP indicates the number of swirl pairs for a given ring. For a single swirling structure, SP is 0.5 while for a single pair such as twin vortices, the SP value is 1. The methodology to compute the swirl distortion descriptors is the same as in Tanguy et al. (2017). The instantaneous ring-based distortion descriptors are computed and area-averaged to obtain a single descriptor (SI, SP and SD) per snapshot. Therefore, the distortion assessment at the AIP for the experimental and numerical data is performed using the exact same post-processing tools. The distortion is computed over 9 rings and 72 rakes for both CFD and experimental data.

For the baseline configuration, a total of 86 convective times (τ_c) which is equivalent to 0.3s, is used for the comparison with the experimental data. Although the sampling acquisition for the experimental and the ZDES results are significantly different (80 kHz for the ZDES compared with 3.5Hz for the S-PIV measurements), the statistics of the distortion descriptors provide a relevant comparison as the statistics for both datasets are converged. The distortion descriptors for the ZDES simulation including the flow control devices are computed over 35 τ_c which are sufficient to obtain converged statistics.

For the baseline configuration, the instantaneous flowfield at the AIP shows a distorted flowfield with large deviations from the time averaged flowfield (Figure 17). The time averaged swirl intensity $\langle SI \rangle$ obtained with the ZDES agrees with the experimental data with values of 8.5° and 8.4° respectively. The level of fluctuation based on the standard deviation of the SI temporal signal (σ_{SI}) for the ZDES solution is also close to the experimental data with 1.4° and 1.6° respectively. Previous experimental studies (Gil-Prieto et al., 2018, 2017a) identified the presence of peak swirl distortion events for this type of S-duct geometry associated with bulk swirl pattern which can severely impact the performance of an embedded engine. An S-duct unsteady calculation not only needs to match the averaged and fluctuating levels at the AIP but also to be able to capture those peak events. The S-PIV data demonstrated the presence of maximum swirl distortion events associated with bulk vortices at the AIP with maximum SI value up to 13.6° (Figure 17a). Similar events could also be identified for the ZDES solution as illustrated in Figure 17b with the presence of a clockwise bulk swirl (negative swirl angle) at the AIP associated with a maximum value of SI of 14.5° (Figure 17c, event 3). Interestingly, a bulk swirl event with peak value of SI is not necessarily associated with a minimum total pressure ratio (PR) value (Figure 17c) which demonstrates the need to include the assessment of the distortion based on both total pressure and swirl flowfields for the design of an intake.

The probability distributions of the SI signals for the ZDES and S-PIV are compared with the higher order statistics such as the skewness and kurtosis. For the baseline configuration, both SI signals have a distribution with a kurtosis close to the normal distribution value of 3.0. A positive skewness of 0.46 for the S-PIV and 0.41 for the ZDES also indicates that the SI signal is correctly reproduced by the CFD simulation at the AIP (Figure 18).

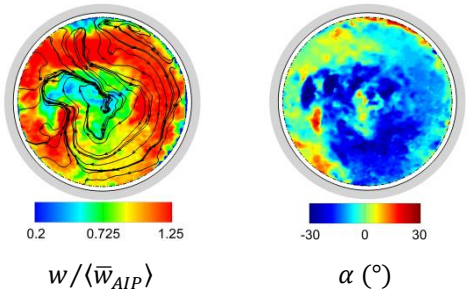

a) SPIV snapshot of a contra-rotating bulk swirl event (clockwise)

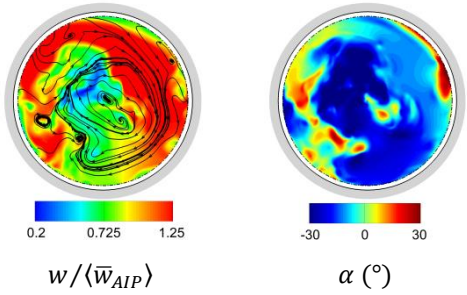

b) ZDES instantaneous flow solution of a contra-rotating bulk swirl event (clockwise)

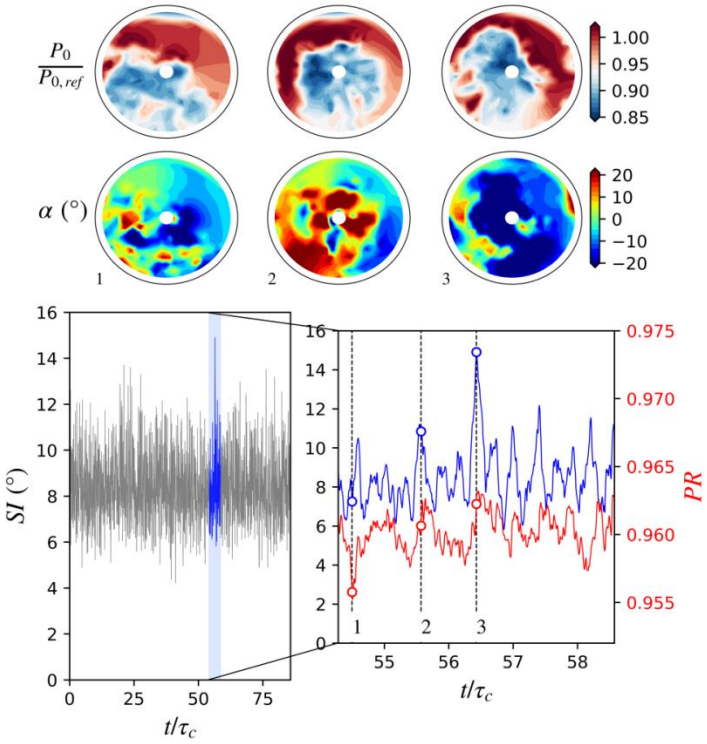

c) Temporal signal of the Swirl Intensity and Pressure ratio at the AIP based on ZDES results

Figure 17 Illustration of the ZDES SI signal and extreme bulk swirl event at the AIP for the baseline configuration

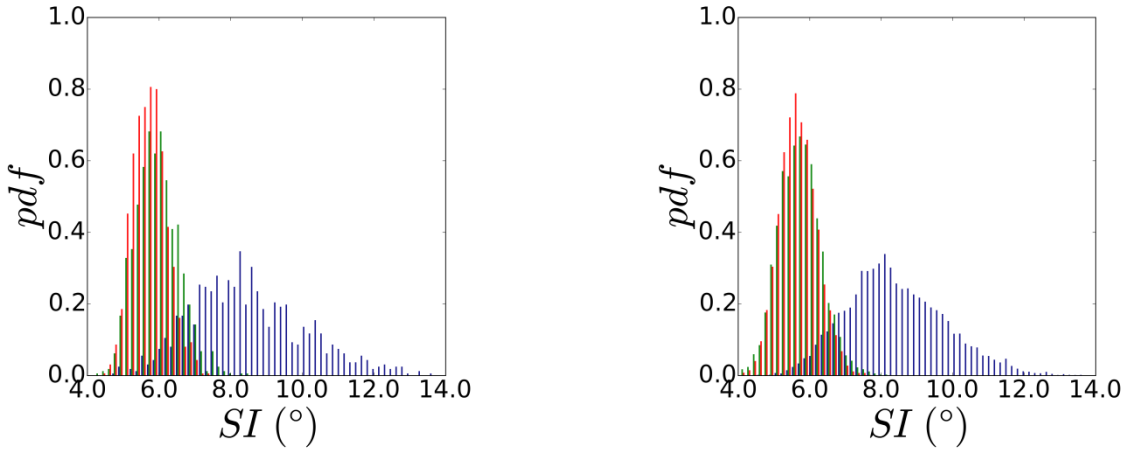

a) S-PIV measurements b) ZDES data

Figure 18 Normalised PDF of the Swirl intensity (SI) for the baseline (blue), VGR1 (green) and VGR5 (red) and from S-PIV and ZDES data

A joint probability map is computed with the swirl distortion descriptors to evaluate the inter-relationship between the distortion descriptors (Figure 19, Figure 20). The axis of each descriptor has been discretised in 100 equi-spaced partitions which provide a spatial resolution of 0.16, 0.02 and 0.02 for SI, SD and SP respectively. For the baseline configuration, the swirl switching mechanism promotes the occurrence of bulk swirl events at the AIP (Gil-Prieto et al., 2017a). This is

characterised by SP and SD values close to 0.5 and |1|, respectively. A twin swirl pattern can also be identified by events where SP and SD equal to 1 and 0.0 respectively. Both of these types of distortion events identified for the S-PIV are captured by the CFD (Figure 20). The highest values of swirl intensity are achieved for large values of absolute swirl directivity which agreed with the S-PIV results (Figure 19). The computed unsteady characteristics of the swirl distortion descriptors SD are also remarkably close to the experiment. The presence of multiple bulk swirl events within the flowfield at the AIP for the CFD calculation is clearly identified by the cloud maps and associated with the large values of SI (Figure 19d). Therefore, based on the swirl distortion descriptors, the ZDES results demonstrate a good agreement with the experiment and reproduce not only the correct time averaged level of distortion but also the main flow dynamics responsible for the peak swirl events at the AIP.

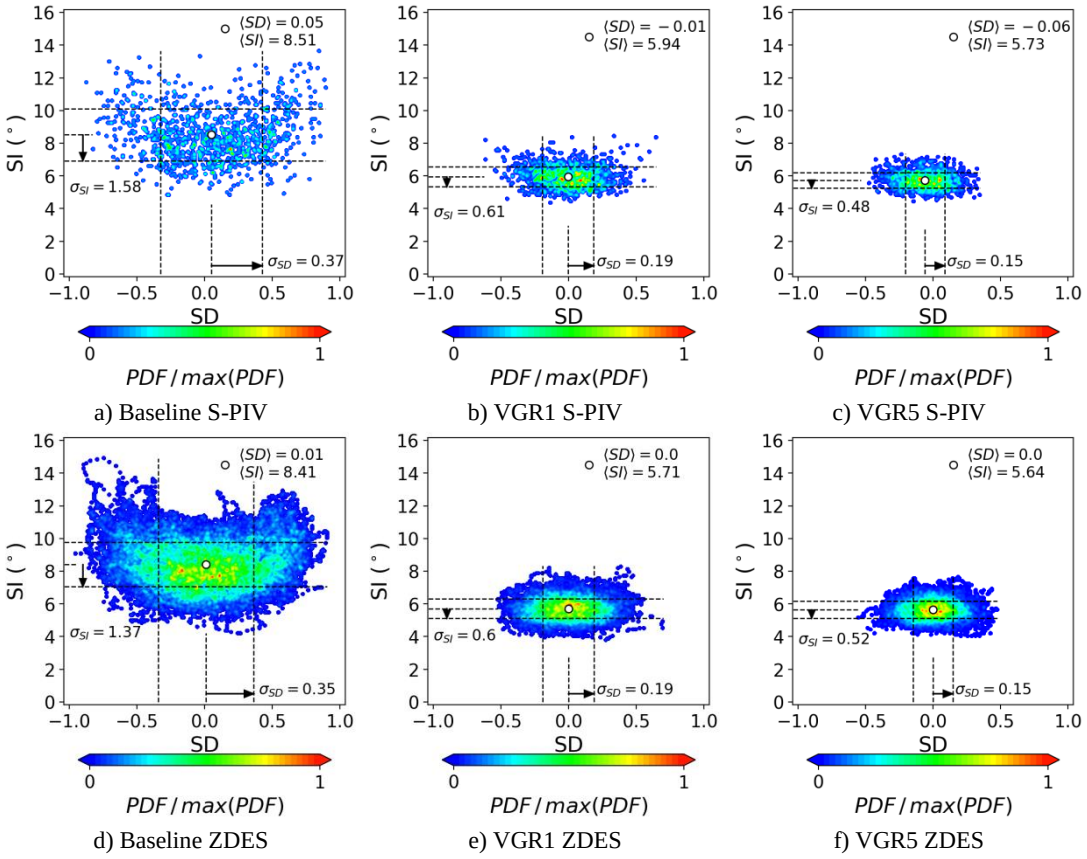

a) Baseline S-PIV b) VGR1 S-PIV c) VGR5 S-PIV

d) Baseline ZDES e) VGR1 ZDES f) VGR5 ZDES

Figure 19 Comparison of the baseline and the VG configuration of the SD − SI joint probability cloud maps

The use of vortex generators considerably modifies the unsteady flowfield at the AIP and can contribute to the reduction of both the total pressure loss and swirl distortion (Tanguy et al., 2017). For the S-PIV flowfield the use of VGR1 and VGR5 reduces the time averaged swirl intensity value $\langle SI \rangle$ by 31% and 33% respectively (Figure 19a, b and c). For the ZDES, the use of the vortex generators also reduces the mean swirl intensity with $\langle SI \rangle = 5.7°$ and 5.6° for VGR1 and VGR5 compared with 8.4° for the baseline configuration (Figure 19d, e and f). Therefore the ZDES predicts a reduction in $\langle SI \rangle$ of 32% and 33% for VGR1 and VGR5 compared with the baseline configuration which agrees with the S-PIV measurements. Based on the experimental results, the use of vortex generators reduces the level of flow fluctuations at the AIP which directly impacts the standard deviation of the swirl intensity σ_{SI}. For both S-PIV and ZDES results, the level of σ_{SI} is equal to 0.6° and 0.5° for VGR1 and VGR5 respectively which demonstrates the capability of the ZDES to correctly model the unsteady flowfield at the AIP (Figure 19). Thus, the ZDES predicts a reduction of the fluctuation levels of SI

(σ_{SI}) of 56% and 62% for VGR1 and VGR5 respectively compared with the baseline. Although the kurtosis of the SI signal is close to the normal distribution for the baseline and the VGs configurations, the reduction in standard deviation (σ_{SI}) for the VGs increases the probability of obtaining SI values close to $\langle SI \rangle$. A similar probability density function (PDF) is obtained for the ZDES results compared with the S-PIV flowfield for the baseline and the VG configurations (Figure 18).

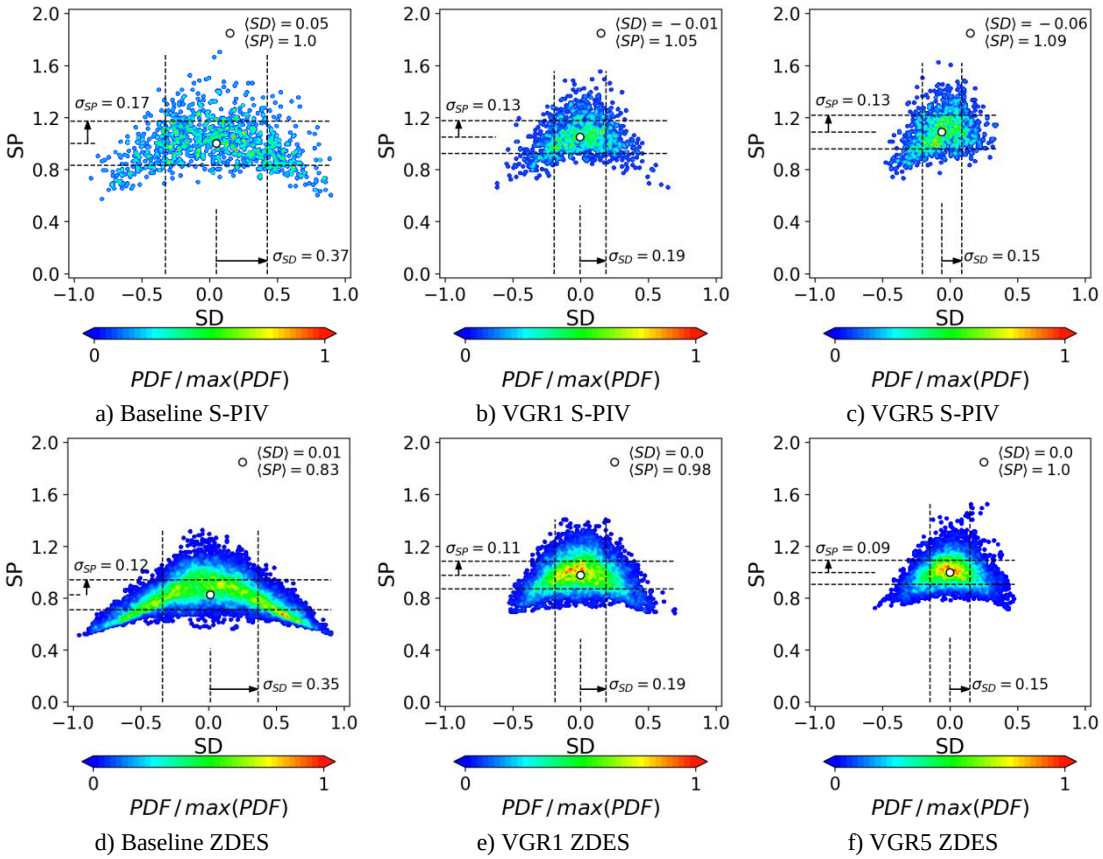

a) Baseline S-PIV b) VGR1 S-PIV c) VGR5 S-PIV

d) Baseline ZDES e) VGR1 ZDES f) VGR5 ZDES

Figure 20 Comparison of the baseline and the VG configuration of the SD−SP joint probability cloud maps

In addition to the level of fluctuations, the ability for the ZDES to predict maximum levels of swirl distortion is a major requirement as peak swirl events can trigger engine surge. For the baseline configuration, the ZDES successfully models the presence of peak swirl events at the AIP. The reduction of maximum swirl intensity caused by the use of vortex generators is also well calculated by the ZDES with a maximum SI value of 8.3° and 7.6° for VGR1 and VGR5 compared with 8.5° and 7.4° for the S-PIV flowfield (Figure 19). As for the baseline, the assessment of SP and SD are used to identify the flow pattern associated with a given value of SI (Figure 20). When the vortex generators are used, the flowfield is stabilised and the fluctuating levels of the SD descriptors or reduced by 46% and 57% for VGR1 and VGR5 respectively. The standard deviation of the swirl directivity (σ_{SD}) for the ZDES is identical to the one computed from the S-PIV flowfield for both VG configurations with $SD = 0.19$ for VGR1 and 0.15 for VGR5 (Figure 20).

The range of SD values calculated from the CFD for VGR1 is also in agreement with the experimental data. For VGR5, the range of SD value is between -0.5 and 0.35 for the S-PIV data while for the ZDES, SD = [-0.50:0.48] (Figure 19c and d). The narrower range in SD value for the experimental results is explained by the presence of a small asymmetry at the AIP flowfield (Figure 15) which tends to bias the flowfield toward one side for VGR5. The suppression of bulk swirl events characterised by $SP \cong 0.5$ and $|SD| \cong 1$ (Figure 19a and d) by the vortex generators is also reproduced by the ZDES. As

a result, peak swirl events identified for the baseline configuration are no longer associated with high value of $|SD|$ (Figure 19).

Therefore the ZDES can be used to estimate the time averaged and fluctuating levels of swirl distortion at the AIP for an S-duct with and without vortex generators. The effect of flow control over the mean distortion at the AIP is well captured by the ZDES which predicted a reduction of the order of 30% in swirl intensity levels similar to the experimental results. The effect of the VGs on the unsteady distortion was also correctly calculated by the ZDES with a maximum decrease in swirl fluctuations of 62% as for the experiment.

5. Conclusion

The Zonal Detached Eddy Simulation method has been used to investigate the effect of passive flow control devices applied within a high offset duct ($H/L = 0.49$) for a reference Mach number of 0.60. The validation of the CFD method has been performed with an extensive experimental data set made of total pressure and S-PIV measurements at the Aerodynamic Interface Plane (AIP). For the baseline configuration, the ZDES solution demonstrated a switch from RANS to LES model after the primary flow separation. Despite a short delay in the development of the instabilities after the separation, the level of unsteadiness at the AIP was in agreement with the experimental results. The use of vortex generators promoted a rapid switch from RANS to LES by generating a set of vortices close to the wall and by introducing flow unsteadiness. The use of the Chimera grid to implement the VGs enabled the local refinement of the grid and captured the unsteady wake of the VGs. The passive flow control devices completely restructure the flowfield by suppressing the main separation region within the S-duct and by preventing the rise of the initial primary secondary flows. The change in time averaged and fluctuating flowfield at the Aerodynamic Interface Plane (AIP) due to the use of vortex generators is properly reproduced by the ZDES. The mean and fluctuating levels of total pressure, velocity and swirl at the AIP were in agreement with the experimental data for the configurations without and with the VGs. As a result, the CFD simulation successfully predicted the change in intensity and distribution of the losses at the AIP due to the flow control devices.

The assessment of the flowfield based on joint-probability maps of the swirl distortion descriptors SP, SD and SI demonstrated that the ZDES can reproduce the statistical distribution of the unsteady flow topology classification at the AIP. For the baseline configuration, the ZDES results showed a similar relationship between the swirl pairs and swirl directivity unsteadiness as the one identified by the S-PIV measurements. The unsteady CFD is able to reproduce the correct level of swirl distortion associated with the swirl switching mechanism for the baseline. Furthermore, the ZDES calculation also demonstrates the ability to reproduce the topology of extreme swirl distortion events associated with the correct level of swirl intensity previously identified from the experimental data. The mean and standard deviation of the swirl intensity were predicted within 1% and 13% error respectively compared with the experiment. The experimental and CFD solutions demonstrated a reduction of about 30% in mean swirl intensity $\langle SI \rangle$ when the flow control devices are used. The reduction in fluctuating levels of SI is also well captured by the CFD with a decrease of the order of 62% in σ_{SI} compared with 65% for the experimental results. As for the experimental measurements, the ZDES with flow control devices suppresses the large excursions from the mean events present in the baseline configuration. As a result the flowfield remains more stable with confined regions of unsteadiness driven by the vortices generated by the devices.

Therefore, the AIP unsteady flowfield for a high offset S-duct was successfully reproduced by the Zonal Detached Eddy Simulation with the Chimera method with and without flow control devices. However, an initial knowledge of the flow field and experience in hybrid RANS/LES computation are useful to ensure the correct use of the model for intake

flows. This study demonstrates that the ZDES can be used to estimate the performance of a flow control device based on the swirl distortion metrics, which is essential for intake design purposes.

6. References

Anderson, B.H., Gibb, J., 1993. Study on vortex generator flow control for the management of inlet distortion. Journal of Propulsion and Power 9, 422–430. https://doi.org/10.2514/3.23638

Berens, T.M., Delot, A., Chevalier, M., Van Muijden, J., 2014. Numerical simulations for high offset intake diffuser flows, in: 52nd AIAA Aerospace Sciences Meeting - AIAA Science and Technology Forum and Exposition, SciTech 2014. American Institute of Aeronautics and Astronautics, National Harbor, Maryland, US. https://doi.org/10.2514/6.2014-0371

Blanc, F., 2010. Patch Assembly: An Automated Overlapping Grid Assembly Strategy. Journal of Aircraft 47, 110–119. https://doi.org/10.2514/1.44116

Boniface, J.C., Joubert, G., Pape, A.L., 2013. Passive Flow Control by Vortex Generators for Internal and External Aerodynamics Configurations, in: 48th International Symposium of Applied Aerodynamics, AIAA Aviation Forum. American Institute of Aeronautics and Astronautics, pp. 25–27.

Burrows, T.J., Vukasinovic, B., Glezer, A., Lakebrink, M.T., Mani, M., 2021. Experimental and numerical investigation of active flow control of a serpentine diffuser. AIAA Journal 59, 607–620. https://doi.org/10.2514/1.J059533

Burrows, T.J., Vukasinovic, B., Lakebrink, M.T., Mani, M., Glezer, A., 2019. Control of flow distortion in offset diffusers using trapped vorticity. International Journal of Heat and Fluid Flow 75, 122–134. https://doi.org/10.1016/j.ijheatfluidflow.2018.11.003

Charonko, J.J., Vlachos, P.P., 2013. Estimation of uncertainty bounds for individual particle image velocimetry measurements from cross-correlation peak ratio. Measurement Science and Technology. https://doi.org/10.1088/0957-0233/24/6/065301

Chauvet, N., Deck, S., Jacquin, L., 2007. Zonal Detached Eddy Simulation of a Controlled Propulsive Jet. AIAA Journal 45, 2458–2473. https://doi.org/10.2514/1.28562

Connolly, B.J., Loth, E., Frederic Smith, C., 2022. Unsteady Separated Flows in an S-Duct and a Bifurcating Duct. Journal of Aircraft. https://doi.org/10.2514/1.c036383

Connolly, B.J., Loth, E., Smith, C.F., 2018. Unsteady flow simulations for diffusing s-ducts of circular and rectangular cross-section, in: AIAA Aerospace Sciences Meeting, 2018. https://doi.org/10.2514/6.2018-2130

Cummings, R.M., Liersch, C., Schuette, A., 2018. Multi-Disciplinary Design and Performance Assessment of Effective, Agile NATO Air Vehicles, in: 2018 Applied Aerodynamics Conference, AIAA Aviation Forum. American Institute of Aeronautics and Astronautics. https://doi.org/10.2514/6.2018-2838

Deck, S., 2011. Recent improvements in the Zonal Detached Eddy Simulation (ZDES) formulation. Theoretical and Computational Fluid Dynamics 26, 523–550. https://doi.org/10.1007/s00162-011-0240-z

Deck, S., Renard, N., Laraufie, R., Sagaut, P., 2014. Zonal detached eddy simulation (ZDES) of a spatially developing flat plate turbulent boundary layer over the Reynolds number range 3 150 $\leqslant$ Reθ $\leqslant$ 14 000. Physics of Fluids 26, 025116. https://doi.org/10.1063/1.4866180

Deck, S., Weiss, P., Pamiès, M., Garnier, E., 2011. Zonal Detached Eddy Simulation of a spatially developing flat plate turbulent boundary layer. Computers & Fluids 48, 1–15. https://doi.org/10.1016/j.compfluid.2011.03.009

Delot, A., Berens, T.M., Tormalm, M.H., Säterskog, M., Ceresola, N., 2014. DES Computations for a Subsonic UAV Configuration with a Highly Integrated S-Shaped Intake Duct, in: 52nd Aerospace Sciences Meeting, AIAA SciTech

Forum. AIAA. https://doi.org/10.2514/6.2014-0723

Delot, A., Garnier, E., Pagan, D., 2011. Flow control in a high-offset subsonic air intake, in: 47th AIAA/ASME/SAE/ASEE Joint Propulsion Conference and Exhibit 2011. American Institute of Aeronautics and Astronautics, San Diego, California, US. https://doi.org/10.2514/6.2011-5569

Delot, A., Scharnhorst, R., 2015. Computational and Experimental Results for Flows in a Diffusing S-Duct without and with Flow Control Devices, in: 51st AIAA/SAE/ASEE Joint Propulsion Conference, Propulsion and Energy Forum. American Institute of Aeronautics and Astronautics. https://doi.org/10.2514/6.2015-3964

Edefur, H., Tormalm, M.H., 2018. Design and Integration of a Low Observable Intake for the MULDICON Platform, in: 2018 Applied Aerodynamics Conference, AIAA Aviation Forum. American Institute of Aeronautics and Astronautics. https://doi.org/10.2514/6.2018-3162

Edwards, J.R., Liou, M.-S., 1998. Low-diffusion flux-splitting methods for flows at all speeds. AIAA Journal 36, 1610–1617. https://doi.org/10.2514/3.14013

Florea, R. V., Matalanis, C., Hardin, L.W., Stucky, M., Shabbir, A., 2015. Parametric Analysis and Design for Embedded Engine Inlets. Journal of Propulsion and Power. https://doi.org/10.2514/1.B34804

Garnier, E., 2015. Flow Control by Pulsed Jet in a Curved S-Duct: A Spectral Analysis. AIAA Journal 53, 2813–2827. https://doi.org/10.2514/1.J053422

Gear, C.W., 1971. Algorithm 407: DIFSUB for Solution of Ordinary Differential Equations [D2]. Communications of the ACM. https://doi.org/10.1145/362566.362573

Georgiadis, N.J., Rizzetta, D.P., Fureby, C., 2010. Large-Eddy Simulation: Current Capabilities, Recommended Practices, and Future Research. AIAA Journal. https://doi.org/10.2514/1.J050232

Gibertini, G., Boniface, J.C., Zanotti, A., Droandi, G., Auteri, F., Gaveriaux, R., Le Pape, A., 2015. Helicopter drag reduction by vortex generators. Aerospace Science and Technology 47, 324–339. https://doi.org/10.1016/j.ast.2015.10.004

Gil-Prieto, D., MacManus, D.G., Zachos, P.K., Bautista, A., 2018. Assessment methods for unsteady flow distortion in aero-engine intakes. Aerospace Science and Technology. https://doi.org/10.1016/j.ast.2017.10.029

Gil-Prieto, D., MacManus, D.G., Zachos, P.K., Tanguy, G., Menzies, K.R., 2017a. Convoluted intake distortion measurements using stereo particle image velocimetry. AIAA Journal 55. https://doi.org/10.2514/1.J055467

Gil-Prieto, D., MacManus, D.G., Zachos, P.K., Tanguy, G., Wilson, F., Chiereghin, N., 2017b. Delayed detached-eddy simulation and particle image velocimetry investigation of S-Duct flow distortion. AIAA Journal 55. https://doi.org/10.2514/1.J055468

Gil-Prieto, D., Zachos, P.K., MacManus, D.G., McLelland, G., 2019. Unsteady characteristics of S-duct intake flow distortion. Aerospace Science and Technology. https://doi.org/10.1016/j.ast.2018.10.020

Giuliani, J.E., Chen, J., 2016. Fan Response to Boundary-Layer Ingesting Inlet Distortions. AIAA Journal 54, 3232–3243. https://doi.org/10.2514/1.J054762

Greitzer, E.M., 1980. Review - Axial compressor stall phenomena. Journal of Fluids Engineering. https://doi.org/10.1115/1.3240634

Hellström, L.H.O., Zlatinov, M.B., Cao, G., Smits, A.J., 2013. Turbulent pipe flow downstream of a 90° bend. Journal of Fluid Mechanics 735. https://doi.org/10.1017/jfm.2013.534

Jacocks, J., Kneile, K.R., 1975. Statistical Prediction of Maximum Time-Variant Inlet Distortion Levels. Tennessee, USA.

Jirásek, A., 2006. Design of vortex generator flow control in inlets. Journal of Aircraft 43, 1886–1892.

https://doi.org/10.2514/1.21364

Jirasek, A., Aref, P., Ghoreyshi, M., Cummings, R.M., Satchell, M., 2018. Computational Design of S-Duct Intakes for the NATO AVT-251 Multi-Disciplinary Configuration, in: 2018 Applied Aerodynamics Conference, AIAA Aviation Forum. American Institute of Aeronautics and Astronautics. https://doi.org/10.2514/6.2018-3164

Kalpakli Vester, A., Örlü, R., Alfredsson, P.H., 2015. POD analysis of the turbulent flow downstream a mild and sharp bend. Experiments in Fluids 56. https://doi.org/10.1007/s00348-015-1926-6

Lakebrink, M.T., Mani, M., 2018. Numerical Investigation of Dynamic Distortion and Flow Control in a Serpentine Diffuser, in: 2018 AIAA Aerospace Sciences Meeting, AIAA SciTech Forum. American Institute of Aeronautics and Astronautics. https://doi.org/10.2514/6.2018-1283

Le Pape, A., Richez, F., Deck, S., 2013. Zonal Detached-Eddy Simulation of an Airfoil in Poststall Condition. AIAA Journal 51, 1919–1931. https://doi.org/10.2514/1.J052235

Liebeck, R.H., 2004. Design of the Blended Wing Body Subsonic Transport. Journal of Aircraft 41, 10–25. https://doi.org/10.2514/1.9084

Mace, J., Lakebrink, M.T., Mani, M., Steenken, W., 2012. Computational Simulation of Dynamic Total-Pressure Distortion in an S-Diffuser, in: 48th AIAA/ASME/SAE/ASEE Joint Propulsion Conference & Exhibit. Altlanta, Georgia, US. https://doi.org/10.2514/6.2012-3999

MacManus, D.G., Chiereghin, N., Prieto, D.G., Zachos, P., 2017. Complex Aeroengine Intake Ducts and Dynamic Distortion. AIAA Journal 55, 2395–2409. https://doi.org/10.2514/1.J054905

Mary, I., Sagaut, P., 2002. Large eddy simulation of flow around an airfoil near stall. AIAA Journal. https://doi.org/10.2514/2.1763

Mary, I., Sagaut, P., Deville, M., 2000. An algorithm for unsteady viscous flows at all speeds. International Journal for Numerical Methods in Fluids 34, 371–401. https://doi.org/10.1002/1097-0363(20001115)34:5<371::AID-FLD54>3.0.CO;2-W

Mayeur, J., Dumont, A., Destarac, D., Gleize, V., 2016. Reynolds-averaged navier-stokes simulations on NACA0012 and ONERA-M6 wing with the ONERA elsA solver. AIAA Journal. https://doi.org/10.2514/1.J054512

McMillan, M.L., Mackie, S.A., Gissen, A.N., Vukasinovic, B., Lakebrink, M.T., Glezer, A., Mani, M., Mace L, J., 2011. Inlet Flow Control and Prediction Technologies for Embedded Propulsion Systems. NASA.

Melling, A., 1997. Tracer particles and seeding for particle image velocimetry. Measurement Science and Technology 8, 1406–1416. https://doi.org/10.1088/0957-0233/8/12/005

Noelting, S., Gautier, S., Wessels, M., Gonzalez, I., 2015. Simulation of an S-Duct Inlet Using the Lattice-Boltzmann Method, in: 51st AIAA/SAE/ASEE Joint Propulsion Conference, Propulsion and Energy Forum. American Institute of Aeronautics and Astronautics. https://doi.org/doi:10.2514/6.2015-3963

Ochs, S.S., Tillman, G., Joo, J., Voytovych, D.M., 2016. Computational Fluid Dynamics-Based Analysis of Boundary Layer Ingesting Propulsion. Journal of Propulsion and Power 33, 522–530. https://doi.org/10.2514/1.B36069

Owens, L.R., Allan, B.G., Gorton, S.A., 2006. Boundary-layer-ingesting inlet flow control, in: Collection of Technical Papers - 44th AIAA Aerospace Sciences Meeting. American Institute of Aeronautics and Astronautics, Reno, Nevada, US, pp. 10091–10113. https://doi.org/10.2514/6.2006-839

Raffel, M., Willert, C., Wereley, S., Kompenhans, J., 2007. Particle Image Velocimetry: a practical guide. Springer-Verlag, Berlin. https://doi.org/10.1007/978-3-540-72308-0

Reichert, B.A., Wendt, B.J., 1996. Improving curved subsonic diffuser performance with vortex generators. AIAA Journal

34, 65–72. https://doi.org/10.2514/3.13022

Richez, F., Le Pape, A., Costes, M., 2015. Zonal detached-eddy simulation of separated flow around a finite-span wing, in: AIAA Journal. https://doi.org/10.2514/1.J053636

Sagaut, P., Deck, S., Terracol, M., 2013. Multiscale and Multiresolution Approaches in Turbulence: LES, DES and Hybrid RANS/LES Methods : Applications and Guidelines. Imperial College Press.

Shur, M.L., Spalart, P.R., Strelets, M.K., Travin, A.K., 2008. A hybrid RANS-LES approach with delayed-DES and wall-modelled LES capabilities. International Journal of Heat and Fluid Flow. https://doi.org/10.1016/j.ijheatfluidflow.2008.07.001

Society of Automotive Engineers, 2017. Inlet Total-Pressure-Distortion Considerations for Gas-Turbine Engines. Warrendale, PA, US. https://doi.org/AIR1419C

Society of Automotive Engineers, 2007. A Methodology for Assessing Inlet Swirl Distortion. Society of Automotive Engineers, Warrendale, PA. https://doi.org/10.4271/AIR5686

Spalart, P.R., 2009. Detached-Eddy Simulation. Annual Review of Fluid Mechanics 41, 181–202. https://doi.org/10.1146/annurev.fluid.010908.165130

Spalart, P.R., Deck, S., Shur, M.L., Squires, K.D., Strelets, M.K., Travin, A., 2006. A new version of detached-eddy simulation, resistant to ambiguous grid densities. Theoretical and Computational Fluid Dynamics 20, 181–195. https://doi.org/10.1007/s00162-006-0015-0

Spalart, P.R., Jou, W.H., Strelets, M.K., Allmaras, S.R., 1997. Comments on the feasibility of LES for wings and on a hybrid RANS/LES approach, in: Proceedings of the 1st AFSOR International Conference on DNS/LES. Ruston, Lousiana, US, pp. 137–147.

Stenning, A.H., 1980. Rotating Stall and Surge. Journal of Fluids Engineering 102, 14–20. https://doi.org/10.1115/1.3240618

Tanguy, G., MacManus, D.G., Garnier, E., Martin, P.G., 2018. Characteristics of unsteady total pressure distortion for a complex aero-engine intake duct. Aerospace Science and Technology 78. https://doi.org/10.1016/j.ast.2018.04.031

Tanguy, G., MacManus, D.G., Zachos, P., Gil-Prieto, D., Garnier, E., 2017. Passive flow control study in an S-Duct using stereo particle image velocimetry. AIAA Journal 55, 1862–1877. https://doi.org/10.2514/1.J055354

Thompson, R.J., Komives, J.R., 2019. Compressible flow through a diffusing serpentine inlet duct assessed with wall-modeled large eddy simulation, in: AIAA Aviation 2019 Forum. https://doi.org/10.2514/6.2019-3702

Tunstall, M.J., Harvey, J.K., 1968. On the effect of a sharp bend in a fully developed turbulent pipe-flow. Journal of Fluid Mechanics 34, 595–608. https://doi.org/10.1017/S0022112068002107

Wellborn, S.R., Okiishi, T.H., 1993. A Study of the Compressible Flow though a Diffusing S-Duct.

Wieneke, B., 2005. Stereo-PIV using self-calibration on particle images. Experiments in Fluids. https://doi.org/10.1007/s00348-005-0962-z

Wojewodka, M.M., White, C., Shahpar, S., Kontis, K., 2018. A review of flow control techniques and optimisation in s-shaped ducts. International Journal of Heat and Fluid Flow 74, 223–235. https://doi.org/10.1016/j.ijheatfluidflow.2018.06.016

Yi, J., Kim, C., Lee, B.J., 2012. Adjoint-based design optimization of vortex generator in an s-shaped subsonic inlet. AIAA Journal 50, 2492–2507. https://doi.org/10.2514/1.J051687

Zachos, P., MacManus, D.G., Gil-Prieto, D., Chiereghin, N., 2016. Flow Distortion Measurements in Convoluted Aero Engine Intakes. AIAA Journal 54, 2819–2832. https://doi.org/10.2514/1.J054904